Retrospective Theses and Dissertations

2001

Photonic bandgap resonators and waveguides

Jonathan Patrick Kavanaugh

Iowa State University

Recommended Citation

INFORMATION TO USERS

This manuscript has been reproduced from the microfilm master. UMI films the text directly from the original or copy submitted. Thus, some thesis and dissertation copies are in typewriter face, while others may be from any type of computer printer.

The quality of this reproduction is dependent upon the quality of the copy submitted. Broken or indistinct print, colored or poor quality illustrations and photographs, print bleedthrough, substandard margins, and improper alignment can adversely affect reproduction.

In the unlikely event that the author did not send UMI a complete manuscript and there are missing pages, these will be noted. Also, if unauthorized copyright material had to be removed, a note will indicate the deletion.

Oversize materials (e.g., maps, drawings, charts) are reproduced by sectioning the original, beginning at the upper left-hand corner and continuing from left to right in equal sections with small overlaps.

Photographs included in the original manuscript have been reproduced xerographically in this copy. Higher quality 6" x 9" black and white photographic prints are available for any photographs or illustrations appearing in this copy for an additional charge. Contact UMI directly to order.

UMI®

Photonic bandgap resonators and waveguides

by

Jonathan Patrick Kavanaugh

A dissertation submitted to the graduate faculty

in partial fulfillment of the requirements for the degree of

DOCTOR OF PHILOSOPHY

Major: Electrical Engineering (Microelectronics)

Major Professor: Gary Tuttle

Iowa State University

Ames, Iowa

2001

UMI Number: 3003250

Copyright 2001 by
Kavanaugh, Jonathan Patrick

All rights reserved.

UMI®

Graduate College
Iowa State University

This is to certify that the Doctoral dissertation of

Jonathan Patrick Kavanaugh

has met the dissertation requirements of Iowa State University

Signature was redacted for privacy.

Major Professor

Signature was redacted for privacy.

For the Major Program

Signature was redacted for privacy.

For the Graduate College

TABLE OF CONTENTS

INTRODUCTION

Photonic bandgap (PBG) structures are periodic dielectric structures which exhibit a frequency band in which electromagnetic waves can not propagate [1]. This allows the use of PBGs as low loss replacements for metals in cavity resonators and waveguides where metal is used to confine electromagnetic radiation.

The field of photonic bandgaps has grown since the publication of the first paper by Yablonovich et. al. [2]. The field is still growing with most of the attention being paid to PBG fabrication to produce PBG structures with bandgaps in the infrared and visible spectra. The two primary applications of photonic bandgaps are cavity resonators and waveguides for optical applications. Although commercial applications of PBG resonators and waveguides at microwave frequencies are yet to be realized, the fabrication of structures for research and development at these frequencies is still important. It is less expensive to fabricate structures at microwave frequencies than at optical frequencies and allows for a proof of concept of resonator and waveguide design, which can be used as a guide in designing at optical frequencies. This thesis covers both Fabry-Perot PBG resonators and PBG waveguides constructed with three-dimensional PBG structures. The dissertation first covers resonators, and then covers waveguides. All attendant electromagnetic theory has been placed into two appendices in order to minimize the repeating of theory common to both parts.

PBG RESONATORS

PBG Structure

PBG structures are electromagnetic-wave band-reject filters. They exhibit a frequency band in which electromagnetic waves can not propagate. The simplest example of a PBG structure is a one-dimensional PBG structure or distributed bragg reflector (DBR) [3]. A DBR is a stack of dielectric layers with the dielectric constants of the layers alternating between high and low values. The thickness of each layer is equal to the wavelength at the center of the band-reject region divided by four times the refractive index of each layer. DBRs are used to construct Fabry-Perot resonators because they can exhibit reflectivity greater than 98% and losses less than 1% [4]. A three-dimensional periodic arrangement of dielectric material can create a PBG structure for waves propagating in all three dimensions, and three-dimensional PBG structures can exhibit reflectivity greater than 99%.

PBG structures can be three-, two-, and one-dimensional, as shown in Fig. 1 [5]-[7]. The bandgap exists in the direction(s) of periodicity. For example, the bandgap in the one-dimensional DBR structure exists only in the z direction, while the bandgap in the two-dimensional DBR structure exists in both the x and y directions. Three-dimensional dielectric PBG structures have been fabricated with bandgaps in the X-Ku-band (8 – 18 GHz, see Fig. 7 on page 16) and W-band (75 – 110 GHz, see Fig. 13 on page 25) spectrum, having measured band gap attenuation of 14 dB (4% transmittance) and 15.5 dB (2.82% transmittance) per unit-cell [8][9] respectively. Two-dimensional PBG structures have been fabricated with bandgaps ranging from the X-Ku-band to the infrared.

Distributed bragg reflectors (DBR), have been fabricated with III-V

semiconductor compounds to produce bandgaps in the infrared spectra. The measured

bandgap attenuation has ranged from 0.6 to 2.4 dB per unit-cell, and the reflectivity has

ranged from 80 to 99.7% for 10 unit-cells. DBRs are used as high-reflectivity mirrors in

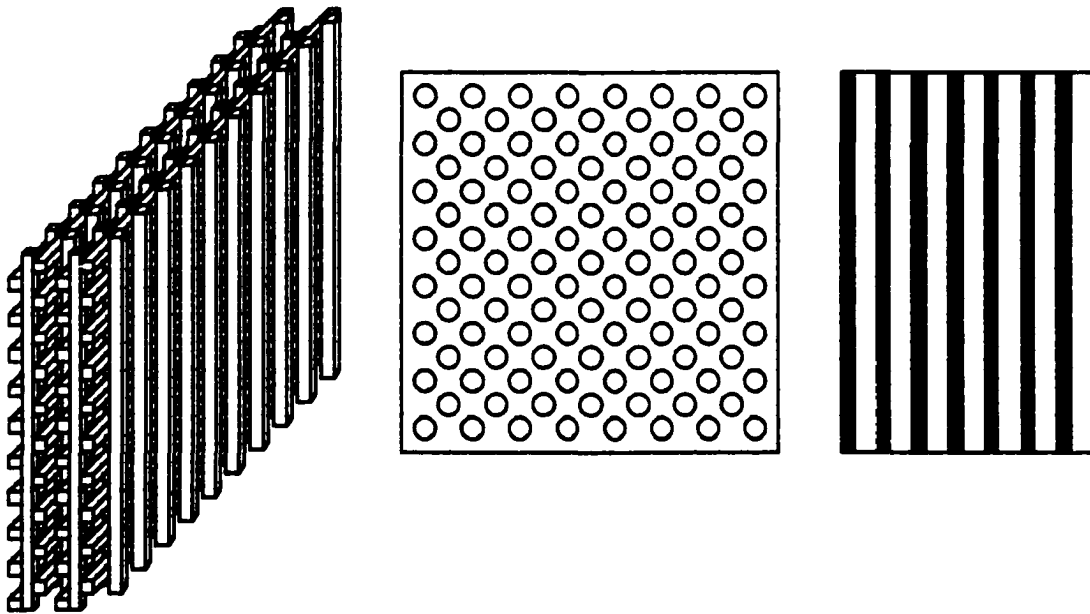vertical cavity lasers and electro-optical switches [10][11].

Figure 1: Examples of three-, two-, and one-dimensional PBG structures.

The three-dimensional PBG structures described in this work will be used as

resonators by fabricating one-dimensional cavities inside the PBG structures. The goal of

this work will be to demonstrate the effectiveness of replacing metal resonators with PBG

counterparts.

The advantages of dielectric PBG resonators over metal resonators include lower absorption and higher Q-factors. The Q-factor of a resonator is the ratio of the resonant frequency to the full-width-half-max (FWHM). The FWHM is the frequency difference between the upper and lower band edges where the transmitted power is one-half the transmitted power at the resonant frequency.

The low absorption within PBG structures allows the use of high-reflectivity PBG mirrors in the construction of one-dimensional Fabry-Perot resonators, because electromagnetic energy transmitted through the high reflectivity PBG structure is greater than the energy absorbed in the PBG structure. Metals cannot be used as high reflectivity mirrors in the construction of Fabry-Perot resonators because the absorption loss is too large.

PBG Resonators

Disadvantages of the PBG resonators are their size and weight. The size of a resonator cavity is proportional to the resonant wavelength, and the size and weight of a resonator's walls (or mirrors) are proportional to the skin depth of the walls. The size and weight of a metal resonator are less than those of the PBG resonator, because the skin depth of the metal is less than the effective skin depth of the PBG structure. The skin depth is defined as the distance at which the power of an electromagnetic wave transmitting through a medium has decreased to 36.8% of the incident power. A W-band (75-110 GHz) PBG structure made of alumina with dimensions 3 cm x 3 cm x 0.47 cm (3 unit cells thick) and weighs 5.28 grams has an attenuation of ~45 dB at the center of the

bandgap. The effective skin depth of the W-band PBG structure is approximately 0.45 mm. A X-Ku-band (11 - 15 GHz) PBG resonator, also made of alumina with dimensions 15.4 cm x 15.4 cm x 4.1 cm and weighs 968 grams has an attenuation of ~43 dB at the center of the bandgap. The effective skin depth of the X-Ku-band PBG structure is approximately 4.1 mm. The volume, weight, wavelength, and skin depth are all approximately nine times larger for the X-Ku-band structure. A sheet of copper with dimensions 15.4 cm x 15.4 cm x 0.16 cm and weights 320 grams has a skin depth of $0.21 \mu m$ in the X-Ku-band and a skin depth of $0.1 \mu m$ in the W-band.

An L-band (1-2 GHz) PBG reflector would require an alumina structure with a volume and weight of approximately 0.9 m^3 and 1000 kg respectively.

Antenna Applications

The size and weight of an L-band resonant detector constructed with PBG reflectors would not be practical when compared to antenna-enhancement structures such as horns and parabolic dishes made of a metal such as copper.

Although the PBG resonator can serve as both an antenna and filter, an inter-digital filter can be added to a horn or parabolic dish and still remain smaller and lighter than the PBG resonator. Size and weight limitations make PBG structures better suited for use in the X-Ku and W bands in applications such as point-to-point communications and automobile collision avoidance systems.

Long range point-to-point communications require directional antennas, which have narrow beam widths. In such applications, a one-dimensional resonator such as a

PBG Fabry-Perot resonator can replace a directional antenna. Short-range communications typically require omni-directional antennas. In such applications, the use of a PBG Fabry-Perot resonator would require a reduction of the gain to increase the beam width. The reduced gain of the resonator would make conventional dipole antennas a more suitable choice.

ONE-DIMENSIONAL PBG STRUCTURES

Due to the high reflectivity and low loss, PBG structures can be used as substrates to enhance the performance of microwave antennas. Conventional substrates act as waveguides and a large percentage of a microstrip antenna's radiated power can be lost in the substrate. The substrate can be thinned to minimize the wave guiding loss, but the strength of the substrate will be compromised. Creating vias in a periodic pattern in a substrate can create a 2-D PBG structure. Two-dimensional PBG structures with a bandgap in the microwave spectra are used as substrates to increase the radiating efficiency of microstrip antennas and can be used to minimize the cross talk between neighboring devices on a microstrip substrate [12].

Parabolic dish and lens antennas with radii 10 times the desired receiving wavelength can enhance the electromagnetic fields incident on a microstrip antenna by 19 dB [13]. In order to achieve enhancement factors greater than this, a PBG resonator would require negligible losses and mirrors with a minimum reflectance of 95%

Assuming that losses due to absorption and scattering in a PBG structures are negligible, a PBG reflectance greater than 95% corresponds to an attenuation greater than 13 dB.

A resonant or defect mode can be created by removing a single rod or a layer of rods from a 2-D or 3-D PBG structure or by removing a layer from a 1-D PBG structure. A defect mode is a narrow frequency band within the bandgap region where electromagnetic waves can propagate. The effect is analogous to forming resonant modes within a Fabry-Perot cavity. Removing a single rod from a 3-D PBG will create a linearly

polarized defect [9]. A 1-D PBG Fabry-Perot resonator is not polarized, but a 3-D PBG

Fabry-Perot resonator can be, as will be shown on page 15.

Distributed Bragg Reflectors

The DBR is the least complex PBG structure to model. The properties of a DBR

with an infinite number of layers, shown in Fig. 2, can be calculated by solving Maxwell's

equation. If there are no free charges, magnetic sources, or sources of loss, the time

independent equation is

$$\nabla^2 \bar{E} = \mu\varepsilon \frac{\partial^2}{\partial t^2} \bar{E} = -\mu\varepsilon\omega^2 \bar{E} \tag{1}$$

By imposing the boundary conditions,

$$\bar{E}(x) = \bar{E}\left(x + a + \sqrt{\varepsilon_r}b\right) \tag{2a}$$

$$\varepsilon_o \bar{E}_1(x = 0) \cdot \hat{x} = \varepsilon_r \bar{E}_2(x = 0) \cdot \hat{x} \tag{2b}$$

$$\varepsilon_o \bar{E}_1(x = a) \cdot \hat{x} = \varepsilon_r \bar{E}_2(x = a) \cdot \hat{x} \tag{2c}$$

$$\varepsilon_o \frac{\partial}{\partial x} \bar{E}_1(x = 0) \cdot \hat{x} = \varepsilon_r \frac{\partial}{\partial x} \bar{E}_2(x = 0) \cdot \hat{x} \tag{2d}$$

$$\varepsilon_o \frac{\partial}{\partial x} \bar{E}_1(x = a) \cdot \hat{x} = \varepsilon_r \frac{\partial}{\partial x} \bar{E}_2(x = a) \tag{2e}$$

The solution to equation 1 is analogous to the solution of the allowed electron energy

levels in a semiconductor crystal. Through analysis of the DBR, a relation between the

PBG properties and the PBG structural dimensions can be determined.

The reflection and transmission of a DBR with a finite number of layers can be solved using the matrix method (see appendix A).

Fabry-Perot Resonators

Although the electromagnetic waves reflecting off a two- or three-dimensional PBG structure at normal incidence are not planar in the near field, the equations for the plane-wave reflectance and transmittance of a PBG Fabry-Perot resonator can still be used as an approximation of the reflectance and transmittance magnitudes. This is because the waves reflected off the PBG structure are planar in the far field.

The reflectance and transmittance of a Fabry-Perot resonator with a region of loss in the cavity are given by equations 3 and 4, which are derived in Appendix A.

$$r = r_0 \exp(-j\phi_{r0}) + \frac{t_1^2 r_2 \exp(-j(2\beta L + \phi_{r1} + \phi_{r2} + 2\phi_{t1} - j2\alpha L))}{1 - r_1 r_2 \exp(-j(2\beta L + \phi_{r1} + \phi_{r2} - j2\alpha L))} \tag{3}$$

$$t_T = \frac{t_1 t_2 \exp(-j(\beta L - \phi_{r1} - \phi_{r2} - j\alpha L))}{1 - r_1 r_2 \exp(-j(2\beta L + \phi_{r1} + \phi_{r2} - j2\alpha L))} \tag{4}$$

In equations 3 and 4, $t = \sqrt{T}$, $r = \sqrt{1-T}$, T is the transmittance of a mirror, β is the propagation constant of the cavity medium, and L is the cavity length. The reflectance phase factors of the mirrors are ϕ_{r1} and ϕ_{r2}. The transmission phase factors of the mirrors are ϕ_{t1} and ϕ_{t2}. The FP resonant condition is satisfied when $2\beta L + \phi_1 + \phi_2 = 2m\pi$, where m is an integer representing the resonant mode number.

The reflection phase factors are included in equations 3 and 4, because the PBG crystal reflection phase is polarization and frequency dependent. The frequency of a FP resonant peak is given by equation 5.
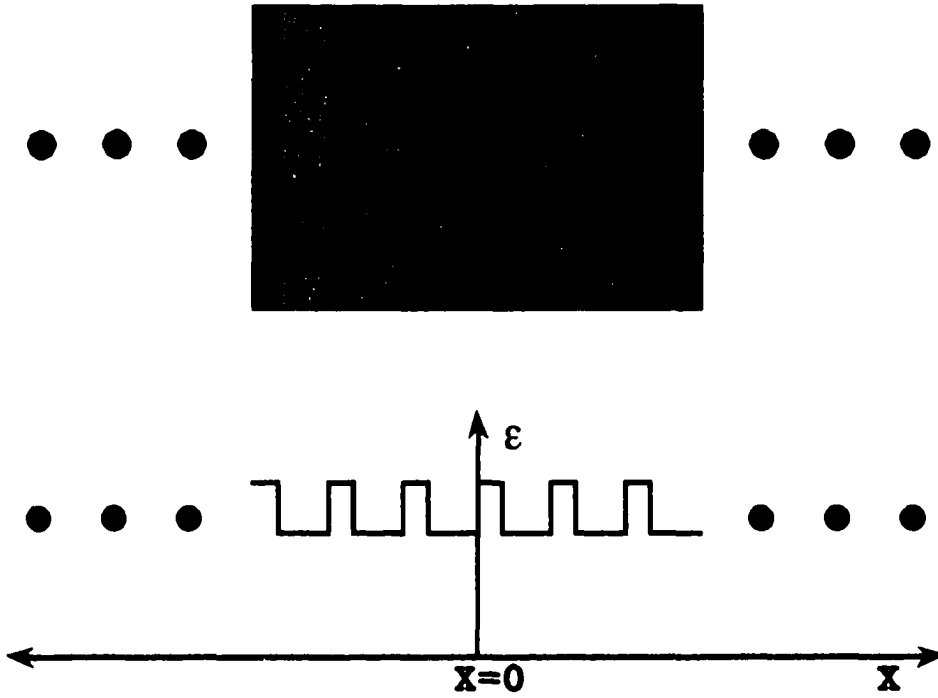
Figure 2: Periodic Structure of a Distributed Bragg Reflector

$$V_{peak} = \frac{m - (\phi_{r1} + \phi_{r2})/2\pi}{2L} \cdot c \tag{5}$$

The conditions for maximum transmission of a FP resonator are identical to the

conditions for minimum reflection. The reflection of a FP resonator, given by equation 3,

is minimum when the FP resonant condition is satisfied and the conditions

$\phi_{t1} + \phi'_{t1} = \phi_0 + (2m + 1)\pi$ and $r_0 = r_1 = r_2$ $(t_1 = t'_1 = t_2)$ are met.

A plot of the theoretical transmission of a Fabry-Perot resonator with mirrors of

equal reflectivity ($r_1 = r_2 = 0.99, 0.95, 0.8,$ and 0.5), a cavity length of 15 mm, and a loss

$\alpha \approx 0$ is shown in Fig. 3. The reflection phases ϕ_{r1}, ϕ_{r2}, ϕ_{t1}, and ϕ_{t2} are all set equal to zero.

Resonator Properties

While the peak transmission remains constant, the quality factor, Q, of the resonant

peak increases with mirror reflection. The Q is the ratio of resonant frequency to the

resonant peak full-width-half-max and is given by equation 6. Equation 6 applies to FP

resonators with identical mirrors having reflectance R_{mirror} [14].

$$Q = \frac{(2m\pi - \phi_1 - \phi_2)\sqrt{R_{mirror}}}{2(1 - R_{mirror})} \tag{6}$$

In a cavity with regions of loss, α is non-zero. As the loss terms in such a cavity

increase, the peak transmission and Q of the resonator will decrease.

The gain of a resonator with loss can be increased by increasing the transmission of

the first mirror while minimizing the transmission of the second mirror. In a

semiconductor Fabry-Perot resonator with loss in the cavity, the gain can be increased by

setting $r1 = r2 \cdot \exp(-\alpha L_{cavity})$ [14]. Changing the transmission of the first mirror can not

increase the Q of a high loss resonator.

In an air-filled FP cavity, the gain of the cavity is the ratio of electric-field

magnitude within the cavity to the field magnitude incident the cavity. The gain is a

function of position within the cavity as shown in equation 6. The derivation of equation 6

is shown in Appendix A. The position, x, has the limits $0 < x < L$.

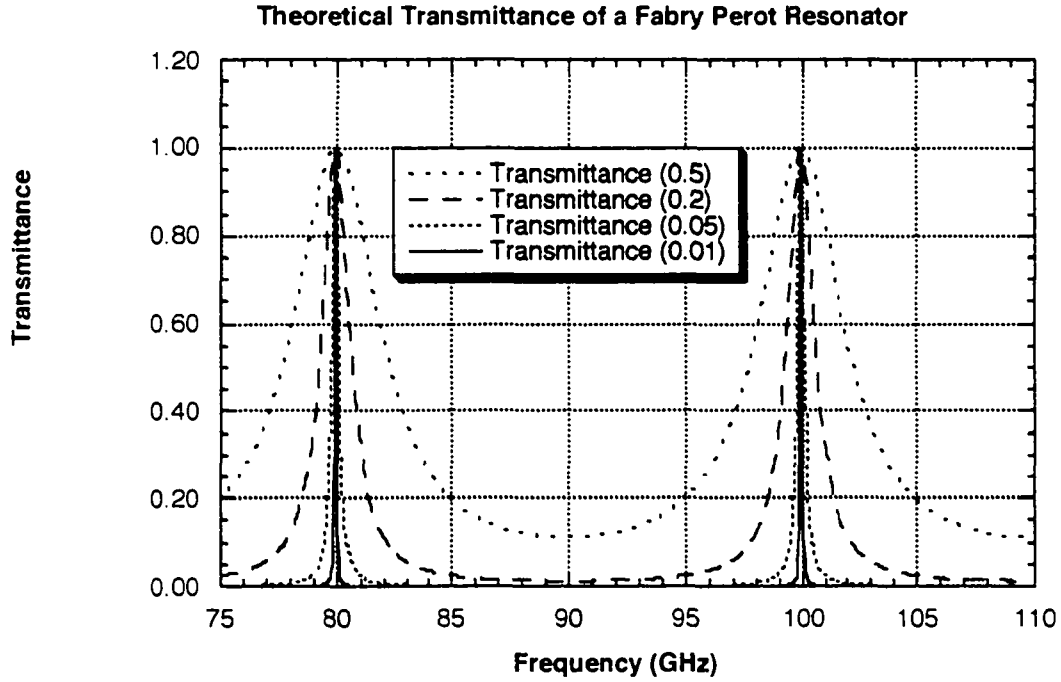**Theoretical Transmittance of a Fabry Perot Resonator**

Figure 3: Calculated transmittance of a FP resonator. The transmittance listed in the key is the transmittance of the resonator's mirrors. The bandwidth of the peaks decreases with mirror transmittance.

$$gain = \left| \frac{E_c(x)}{E_i} \right| = \left| \frac{t_1(\exp(-j\beta x) + r_2 \exp(-j(2\beta L - \beta x - \phi_1)))}{1 - r_1 r_2 \exp(-j(2\beta L + \phi_1 + \phi_2))} \right| \tag{7}$$

To examine the effect absorption has on gain, consider the case $\phi_1 = \phi_2 = 0$ and β is substituted with $\beta - j\alpha$. Under resonant conditions, the maximum gain can be written as
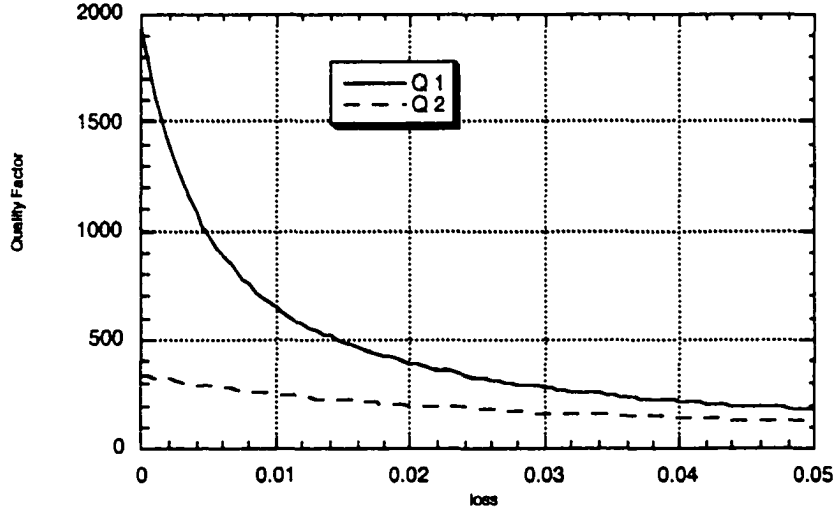
Figure 4: Theoretical Gain of a FP resonator versus loss in the resonator cavity. Gain 1

represents a resonator with the transmittance of both mirrors equal to 0.1. Gain 2

represents a resonator with the transmittance of the mirrors equal to 0.316 and 0.1.

$$gain = \left| \frac{t_1 \left(\exp(-\alpha x) + |r_2| \exp(-\alpha(2L - x)) \right)}{1 - r_1 r_2 \exp(-2\alpha L)} \right| \tag{8}$$

In the case $r_1 = r_2 = 0.995$, $t_1 = \sqrt{1 - r_1^2} = 0.100$, and $x = L$ the theoretical gain is

plotted in Fig. 4 as a function of absorption, αL. Also plotted in Fig. 4, is a second case

$t_1 = \sqrt{t_2}$ (or $1 - r_1^2 = \sqrt{1 - r_2^2}$), $t_2 = 0.100$, $t_1 = 0.316$, and $x = L$.

Notice that for $\alpha L > 0.006$, the gain is greater in the case $t_1 > t_2$ ($r_1 < r_2$). Using

equation 8 to calculate the ratio of the resonance frequency to the FWHM, the modeled Q-

factors for both cases are plotted in Fig. 5 as a function of αL.

Figures 4 and 5 display the pattern of gain and Q decreasing a greater amount when

absorption is added to a resonator with higher mirror reflectivity.
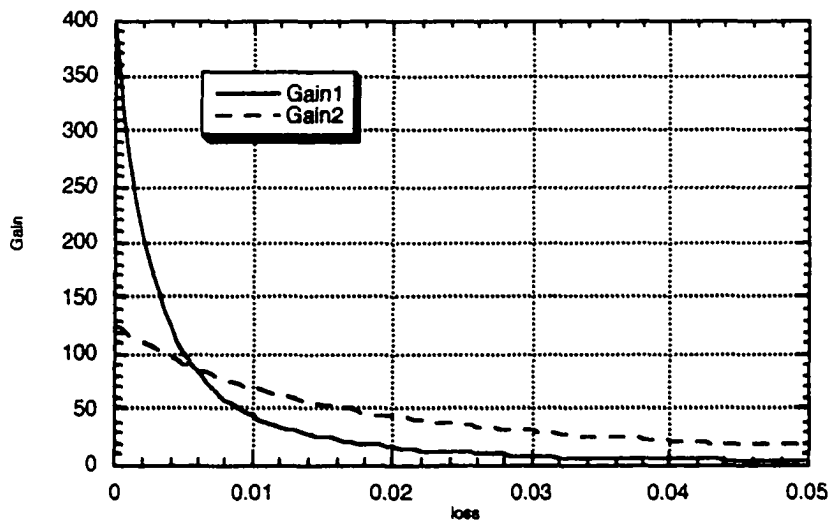

Figure 5: Theoretical Quality Factor of a FP resonator versus loss in the resonator cavity.

The quality factor ,Q1, represents a resonator with the transmittance of both mirrors equal

to 0.1. The quality factor, Q2, represents a resonator with the transmittance of the mirrors

equal to 0.316 and 0.1.

PREVIOUS WORK

X-Ku-Band PBG Properties

The X-Ku-band photonic crystal first demonstrated by Ozbay et. al. is shown in

Fig. 10 on page 19. The experimental setup used to measure the reflection and

transmission of the X-Ku-band PBG is shown in Fig. 6.

The reflection of the X-Ku-band PBG structure was measured in reference to a

metal plate with the same lateral dimensions of the PBG structure. The measured

reflection and transmission magnitudes are shown in Fig. 7. The measured reflection

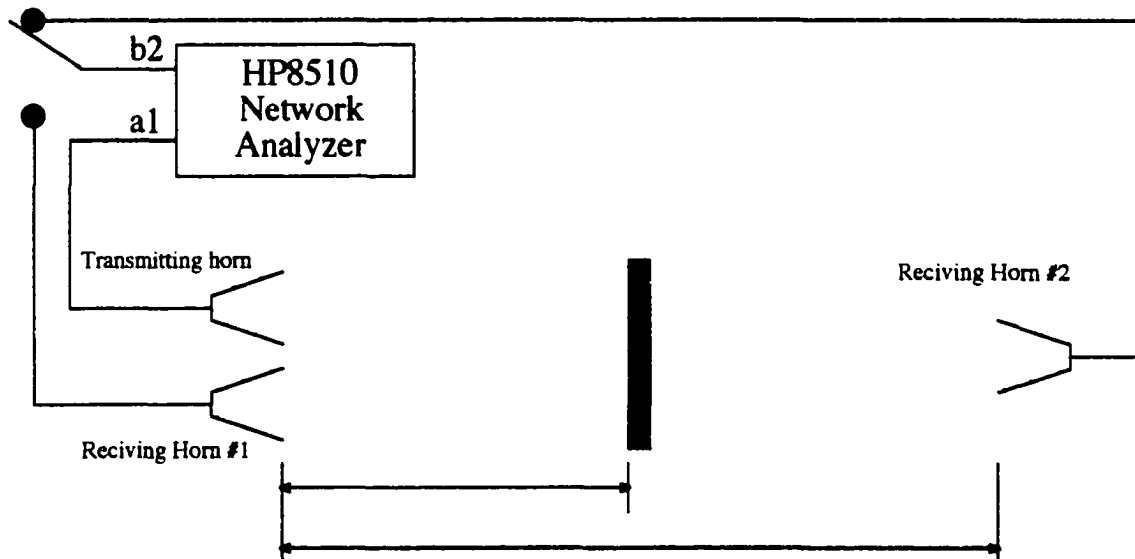phase of both PBG polarizations are shown in Fig. 8.

Figure 6: X-Ku-band Experimental Setup used to measure transmittance and reflectance.

Resonant modes present in the measured reflection (Fig. 7) are due to standing waves formed between the horn antennas and the PBG or metal structure.

To explain why there are two different reflection phases for the two polarizations, consider a PBG structure several unit cells thick with a reflection phase $\phi_1(v)$, which is a function of frequency. The polarization of the PBG structure can be changed by adding one layer of rods to the surface of the PBG and the PBG moved back a distance equal to the thickness of one layer. The new reflection phase $\phi_2(v)$ can be written as

$$\phi_2(v) = \phi_1(v) + \frac{4\pi d}{\lambda} + \Delta\phi_{layer} \tag{9}$$
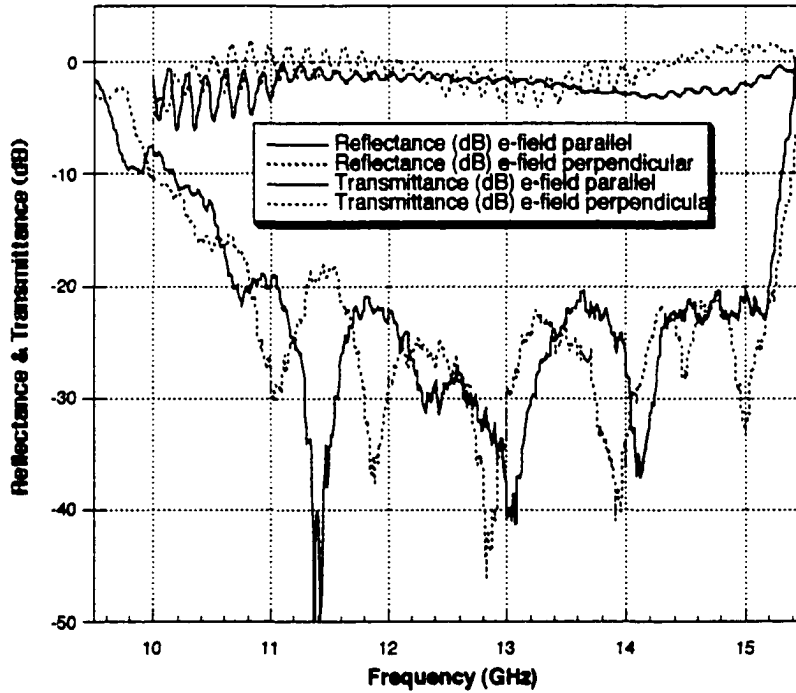

Figure 7: X-Ku-Band PBG Reflectance and Transmittance measured with the incident wave travelling in the rod stacking direction.
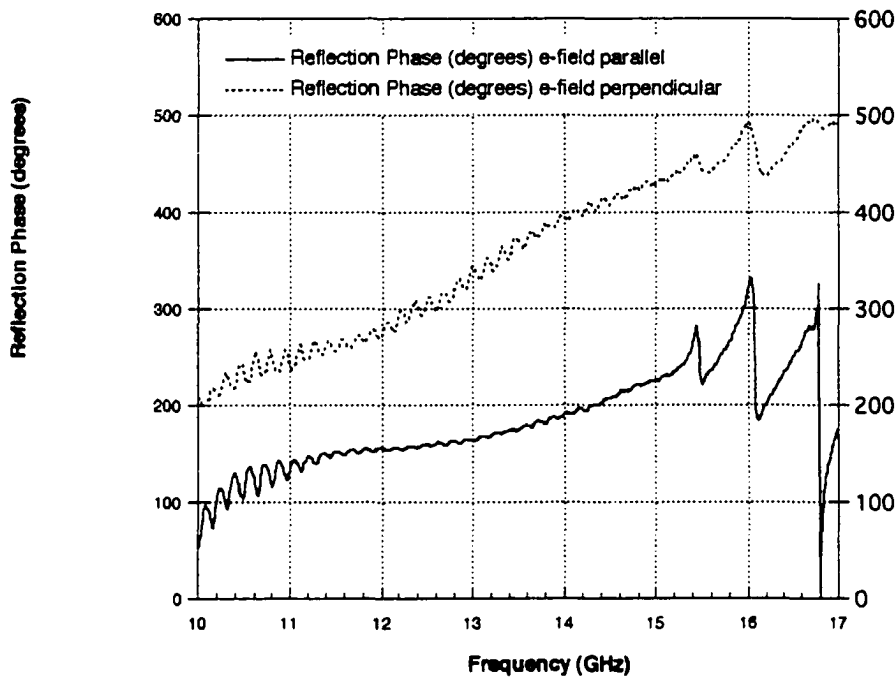
Figure 8: X-Ku-Band PBG Reflection Phase measured with the incident wave travelling in the rod stacking direction.

X-Ku-Band Fabry-Perot Resonator

With a polarization dependant reflection phase, a Fabry-Perot resonator can be constructed which has two unique polarization dependant resonant frequencies as shown in figures 9c and 9d. By rotating one of the PBG structures 90°, a second Fabry-Perot resonator can be constructed with the same PBG structures and same cavity thickness to

produce a third unique resonant frequency for both polarizations as shown in figures 9a

and 9b. Figure 9 illustrated the four possible polarizations and the three effective cavity

thicknesses, which produce the three resonant frequencies. These polarizations will be

used later to measure the PBG reflection phases shown in Fig. 13.

$$\phi_1(\lambda)+\phi_2(\lambda)+2\beta L \qquad \phi_1(\lambda)+\phi_2(\lambda)+2\beta L \qquad 2\phi_1(\lambda)+2\beta L \qquad 2\phi_2(\lambda)+2\beta L$$

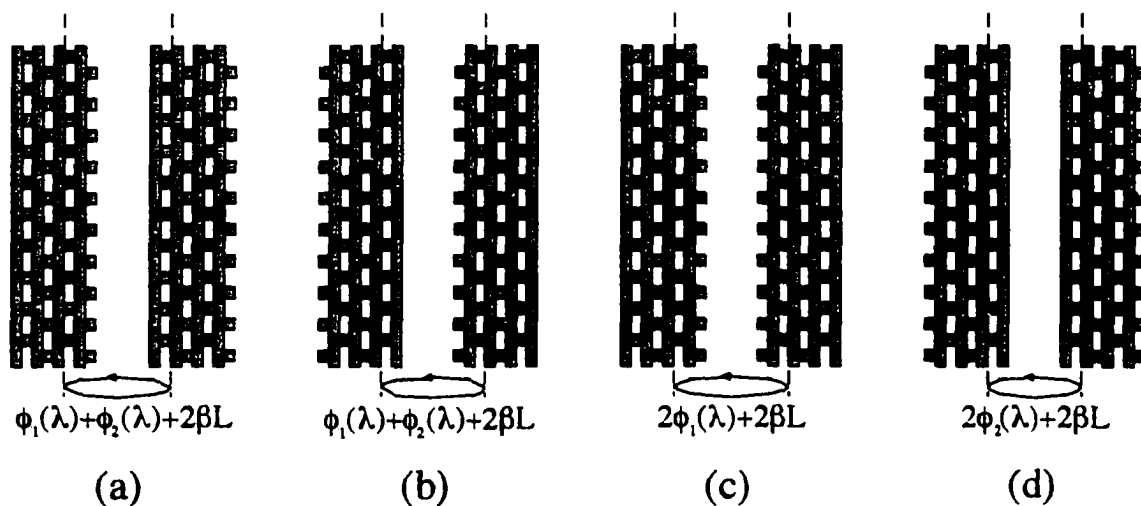(a)   (b)   (c)   (d)

Figure 9: Four possible PBG FP resonator configurations with only one cavity thickness

produce three unique resonant frequencies.

Ozbay et al. demonstrated a resonant cavity enhanced detector embedded in

photonic crystals by inserting a monopole antenna into a photonic crystal FP resonator

[15]. The photonic crystals used by Ozbay exhibit a bandgap from 10.6 GHz to 12.7 Hz,

X-Ku-band. Ozbay reported a power enhancement factor of 450 and a quality factor of

1100 measured with the monopole antenna at a defect frequency of 11.68 GHz. A power

enhancement of 450 corresponds to a gain enhancement of 26.5 dB. The theoretical gain

of a monopole antenna is 1.64 dB, therefore the gain due to the cavity was 28.1 dB.

W-Band PBG Properties

In our Fabry-Perot experiments, we used the W-band photonic crystal shown in Fig. 10, demonstrated by Ho et al [9]. The 3.2 mm thick crystal (8 rod layers) has an attenuation greater than 30 dB and was constructed by stacking laser machined alumina rods. The laser-machined rods are 3.1 cm long with cross-section 0.46 mm x 0.40 mm and a refractive index of 2.86 at 100 GHz. The photonic crystal had a filling ratio of 0.36, and rods. The laser-machined rods are 3.1 cm long with cross-section 0.46 mm x 0.40 mm
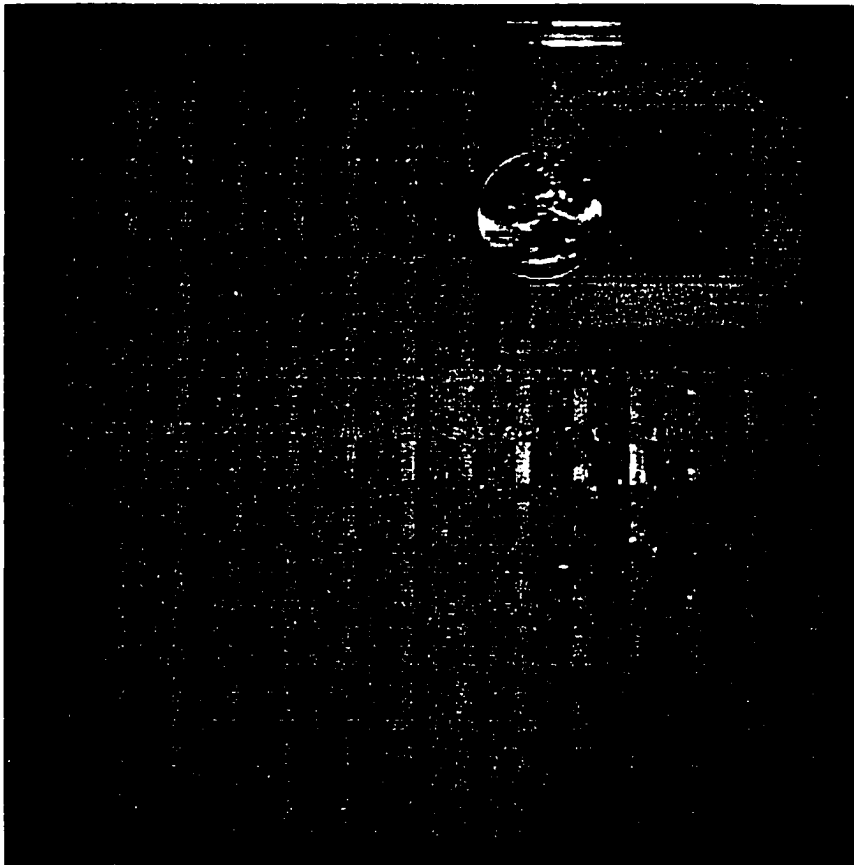

Figure 10: The larger structure is an X-Ku-band PBG crystal and, the smaller is a W-band PBG crystal. A quarter is shown as size reference.

and a refractive index of 2.86 at 100 GHz. The photonic crystal had a filling ratio of

0.36, and each stacking layer was 0.40 mm thick. The mm-wave PBG crystal had a lower

band gap edge at 85 GHz and a band gap attenuation of 15.5 dB per unit-cell. Four

alumina layers make one unit cell. The upper band edge was above 110 GHz, the

frequency limit of the experimental setup. The measured transmittance of the PBG
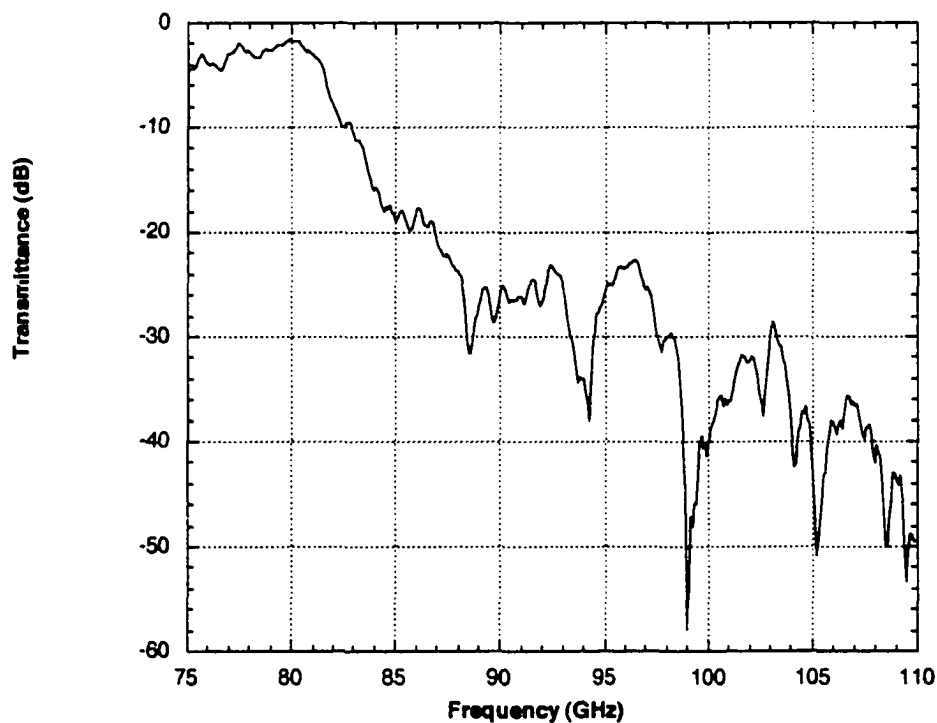
structure is shown in Fig. 11.

Figure 11: Measured transmittance of a W-Band PBG structure illustrating the lower band

edge at ~82 GHz.

W-BAND PBG RESONATORS

Experimental Setup

The experimental setup shown in Fig. 12 allowed transmittance measurements of

PBG crystals but prevented a direct measurement of the PBG crystal reflectance for

incident angles less than 20 degrees. The setup permitted transmittance measurements in

the W-band, 75 GHz to 110 GHz, using an HP8510B network analyzer, two HP

synthesized sweepers, two W-band mixers, a X-Ku-band microwave amplifier, a W-band

mm-wave source, a 10 dB directional coupler, an isolator, and a signal splitter.

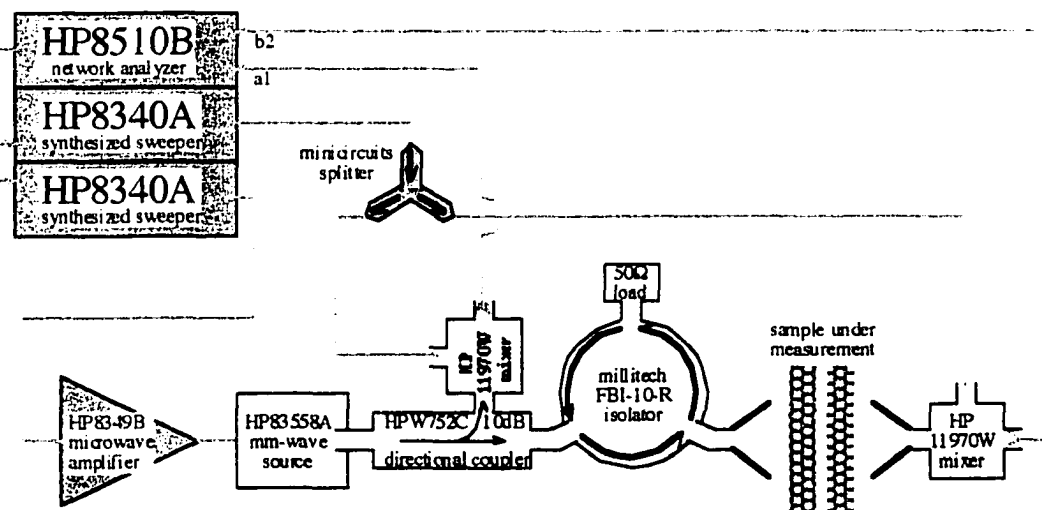Figure 12: W-Band Experimental Setup used to measure transmittance.

One of the synthesized sweepers was used to provide an X-Ku-band local oscillator

signal for the two mixers. The other synthesized sweeper fed an X-Ku-band signal through

the microwave amplifier and on to the mm-wave source. The mm-wave source then

launched a W-band wave into the isolator. The isolator was used to prevent reflected

waves from entering the mm-wave source output. The wave continued from the isolator

into a 10 dB directional coupler. A wave exiting the –10 dB port of the coupler was fed

into one of the mixers. The mixer converted the W-band wave into an X-Ku-band wave,

which was fed into the a1 port of the 8510A. The wave passing through the coupler was

fed into a horn antenna and directed toward the sample to be measured. The wave, which

transmitted through the sample, entered the receiving horn antenna and was directed into

the second mixer, which converted the W-band wave into an X-Ku-band wave. The X-Ku-

band wave was fed into the b2 port of the 8510A. The 8510B used the output of the two

mixers to measure S21 but could not phase lock the signals of the two sources to its internal

oscillator. Instead, each source would lock its own output signal to a 10 MHz reference

fed from the HP8510.

Reflection Phase

To investigate the reflection phase properties of PBG crystals, the resonant

transmittance frequency of a PBG FP resonator was measured as a function of cavity

thickness. Using equation 5, the reflection phase of the PBG crystals can be calculated.

Two eight layer PBG crystals served as the FP mirrors. To measure the reflection phase of

each polarization separately, the two PBG crystals of the FP resonator were oriented such

that the rods on the inside surfaces of the cavity were parallel, as shown in figures 9c and

9d. With the inner rods parallel, the reflection phases of the two PBG crystals will be

equal. Measurements were made with the polarization vector $\bar{e}$ of the incident EM wave

either perpendicular or parallel to the rods on the inside surfaces of the cavity. Using

equation 5 with the condition $\phi_1 = \phi_2$, the reflection phase for each polarization was

calculated from the measured resonant frequency vs. cavity thickness data. The calculated

reflection phase for each polarization is shown in Fig. 13.

To verify the reflection phase data, the two PBG crystals of the FP resonator were

oriented such that the rods on the inside surfaces of the cavity were perpendicular to each

other, as shown in figures 9a and 9b. Using equation 5, the total reflection phase $\phi_1 + \phi_2$

was calculated from the resonant frequency vs. cavity thickness data and compared with

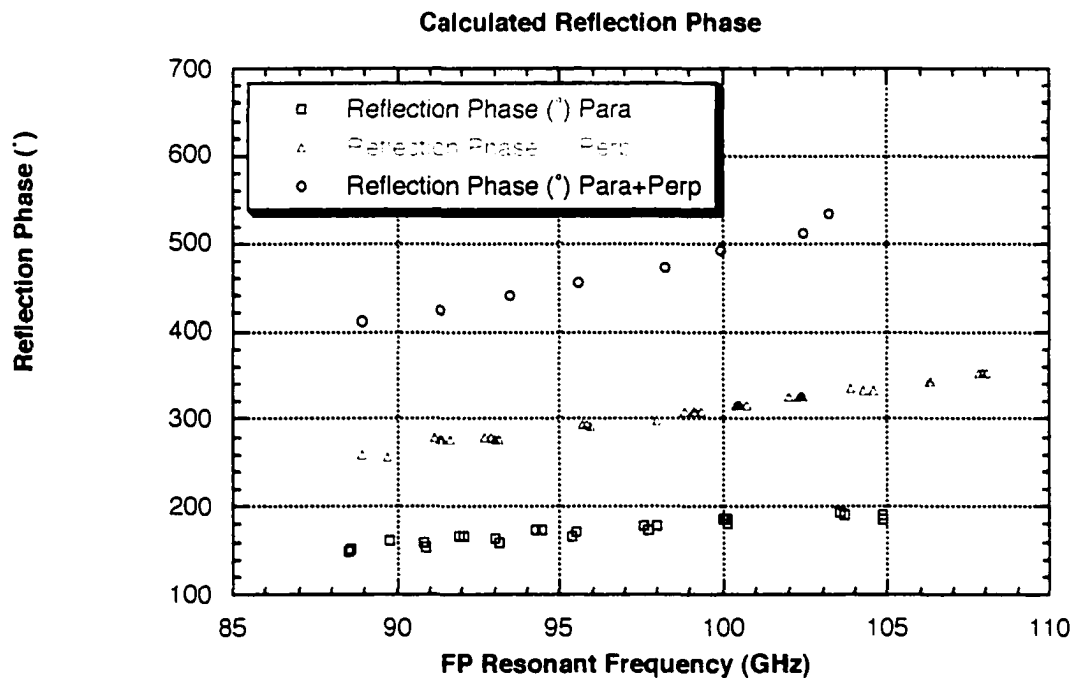the sum of the two reflection phase plots, as shown in Fig. 13.

Calculated Reflection Phase

Figure 13: Calculated reflection phase of the two PBG polarizations and the sum of the two

reflection phases.

Fabry-Perot Resonator Transmission

The measured transmission of a two unit-cell W-band PBG crystal is shown in Fig. 14, and the transmittance data is used to calculate the reflectance of the crystal, assuming negligible absorption loss in the crystal.

Using the reflection phase data in Fig. 13, the calculated reflectance from Fig. 14, and equation 4, the modeled transmittance of a PBG FP resonator with a 0.9-mm cavity is calculated and compared with the measured transmission of a PBG FP resonator, in Fig. 15. The transmission of an ideal FP resonator at resonance is 0 dB. To account for the measured transmission peak maximum of −8.5 dB, loss terms are included in equation 4. The first loss term accounts for the attenuation of air. The maximum attenuation of clean air at 100 GHz is approximated to be 10 dB/km, or $\alpha = 10^{-5}$ dB/mm [16]. Because the cavity is less then 5 mm in length, the attenuation due to air is negligible. A second loss term is introduced by replacing the PBG reflection magnitudes r_1 and r_2 with $r_1(1-\delta)$ and $r_2(1-\delta)$ to account for loss due to imperfect reflection off the PBG. Using $\delta = 0.005$ produces the best agreement between measurement and prediction as illustrated in Fig. 15. The choice of δ corresponds to a 1% loss in reflected power.

There is a 2% error in the modeled resonant frequency. This error is probably due to errors in the measured cavity thickness of this resonator and the resonator used to calculate the reflection phase of the PBG crystals. The measurements of the cavity thickness with the vernier calipers have an error of ±0.02 mm.
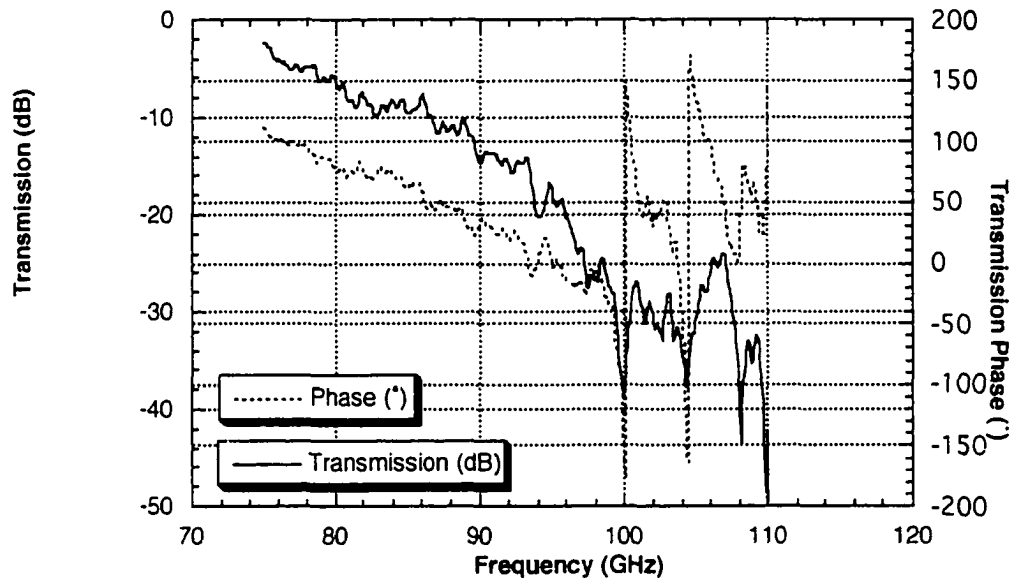
Figure 14: Measured transmittance and transmission phase of a two unit-cell W-band PBG crystal.

The measurement of mm-wave fields inside the FP cavity requires the insertion of a low loss detector less than 1 mm thick into the cavity. A microstrip antenna and high-frequency Schottky-diode detector fabricated on a GaAs substrate were chosen for the detector arrangement.

Inserting a substrate into the cavity pertibates the resonant frequency by increasing the optical thickness of the cavity and adding two air-substrate reflection interfaces to the cavity. The resonant frequency will also change when the substrate is moved about in the cavity in a direction perpendicular to the mirror surfaces. Moving the substrate does not

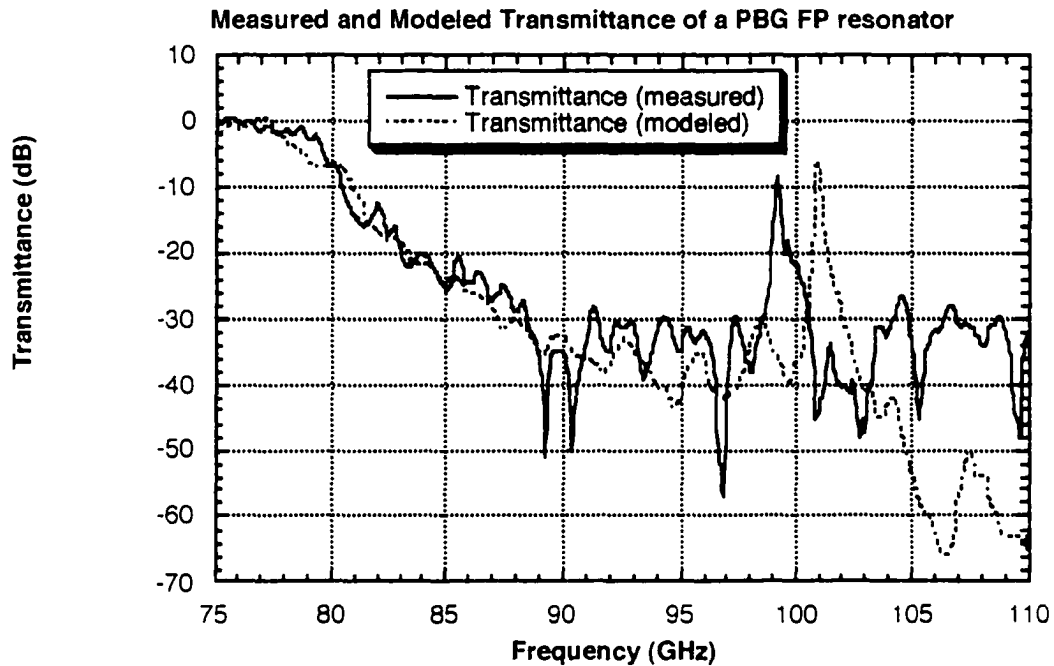**Measured and Modeled Transmittance of a PBG FP resonator**

Figure 15: Measured and modeled transmittance of a PBG FP resonator

change the optical thickness of the cavity, but it does change the locations of the two air-substrate reflection interfaces. In the 3-D PBG Fabry-Perot resonator shown in figures 9a and 9b, the resonant frequencies of the two polarizations are equal. When a substrate is inserted into the cavity, the resonant frequencies of the two polarizations are only equal when the substrate is centered between the two PBG structures of the resonator. Although changing the polarization of the resonator does not change the cavity thickness or the locations of the air-substrate reflection interfaces, the locations of the PBG reflection interfaces change locations.

If a dielectric or semiconductor slab is inserted into the cavity of a FP resonator, simple derivations of analytic solutions to the transmission, reflection, and gain coefficients of the resonator are no longer tractable. Numerical methods must be used to calculate the coefficients. The matrix method is a numerical calculation that is simple to implement with a computer. A more rigorous numerical calculation of the transmission coefficients can be obtained using the Transfer Matrix method (TMM) [17]. The TMM uses the Greens Function to calculate the electromagnetic waves in the near field. With the TMM, if the electric and magnetic fields in the x-y plane at z=0 are known, then Maxwell's equations can be used at a fixed frequency to integrate the wavefield and calculate the electric and magnetic fields in the x-y plane at z=c. The matrix method can only be used with plane waves, while the TMM can be used with any wave.

The e-plane antenna pattern of a free-space dipole antenna has a half-power beam width of 90°. The half power beam width of a dipole antenna on a finite substrate is less than 90° because the antenna pattern is the superposition of the free space dipole antenna pattern with the transmittance versus angle pattern of the finite substrate. As the refractive index of the substrate increases, the beam width of the substrate transmittance versus angle pattern decreases, resulting in a decreasing antenna half-power beam width. With a high refractive index, the shape of the antenna pattern is dominated by the transmittance versus angle pattern of the substrate. In a similar fashion, the dominant factor in the antenna field pattern of an antenna in a high-gain FP resonator is the transmittance versus angle pattern of the FP resonator.

Millimeter-Wave Power Detector

The detector design chosen consists of a dipole antenna connected to a high-frequency GaAs Schottky diode. The size of the diode's active region is minimized in order to maximize the cut-off frequency of the diode.

The cut-off frequency of a diode can be approximated as the reciprocal of the RC time constant. The resistance in the case of a Schottky diode is the resistance of the semiconductor cathode, and the capacitance is the capacitance of the metal-semiconductor contact. Ignoring parasitic resistance, capacitance, and inductance, the cut-off frequency of the diode was calculated according to:

$$v_c = \frac{1}{RC_j} = \frac{1}{RA}\sqrt{\frac{2V_o}{q\varepsilon N_d}} = \frac{1}{24.4\Omega \cdot 0.109\,fF} = 3.75THz, \tag{10}$$

where A is the area of the metal-semiconductor interface, N_d is the density of donor atoms in the semiconductor in the vicinity of the metal interface, ε is the dielectric constant of the semiconductor, and V_o is 0.73V, the built-in voltage across the interface in forward bias.

The Schottky diode active region consists of a 0.6 μm thick N⁻ doped (3×10^{16}cm⁻³) Si GaAs layer above a 0.8 μm thick N⁺ Si doped (6×10^{18}cm⁻³) GaAs layer. Using molecular beam epitaxy (MBE), the layers were grown on a 500 m thick GaAs semi-insulating substrate. A proton implantation process was used to isolate the diode active regions from one another.

The diode active region had a surface area of 144 μm², and was spaced 2000 μm from the neighboring active regions. Wet etching two windows through the N- doped layer and depositing a Ge-Au-Ni GaAs ohmic contact in the windows formed the cathode

ohmic contact. The anode was formed by depositing a 2 μm wide layer of gold on the N-

layer between the two etch windows. The fabrication process is explained in greater detail

in appendix C.

A typical I-V curve for one of the fabricated GaAs Schottky diodes is shown in Fig.

16. A plot of the curve magnified about the origin is shown in Fig. 17. The turn-on

voltage of the diode is about 0.3V as shown in Fig. 17. The diode has an approximately

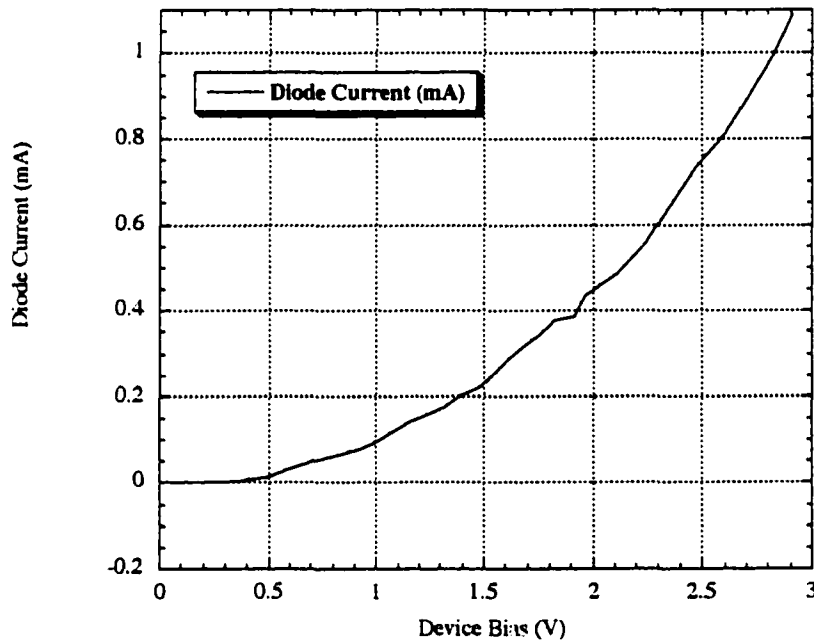linear region from 0 to 0.3V. Because of the linear region, an oscillating field present at

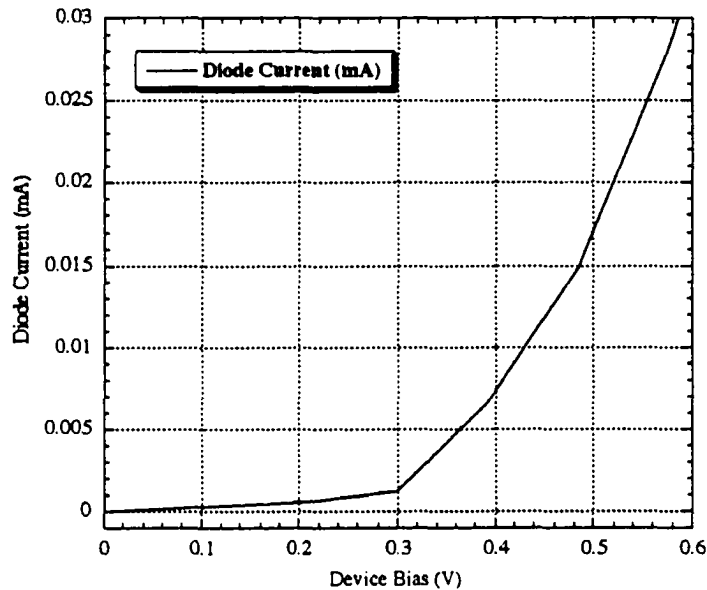Figure 16: I-V curve of a GaAs Schottky Diode with a 2μm x 8μm anode.

Figure 17: Expanded view of the Schottky Diode Turn-on Voltage

the terminals of a 0V biased diode with not significantly change the voltage across the terminals of the diode until the voltage of the oscillating field exceeds 0.3 V.

To investigate the gain and quality factor of the resonant mode within the FP cavity, a mm-wave power detector was placed inside the cavity. The GaAs Schottky-diode design shown in Fig. 18 was selected as the mm-wave power detector. A 1578 m long, 18 m wide quarter-wave dipole antenna was connected to the diode. The antenna had a predicted resonant frequency of 33 GHz [18]. Between 75 GHz and 110 GHz, the dipole antenna behaves as a long dipole antenna. Connections for DC between the diode and
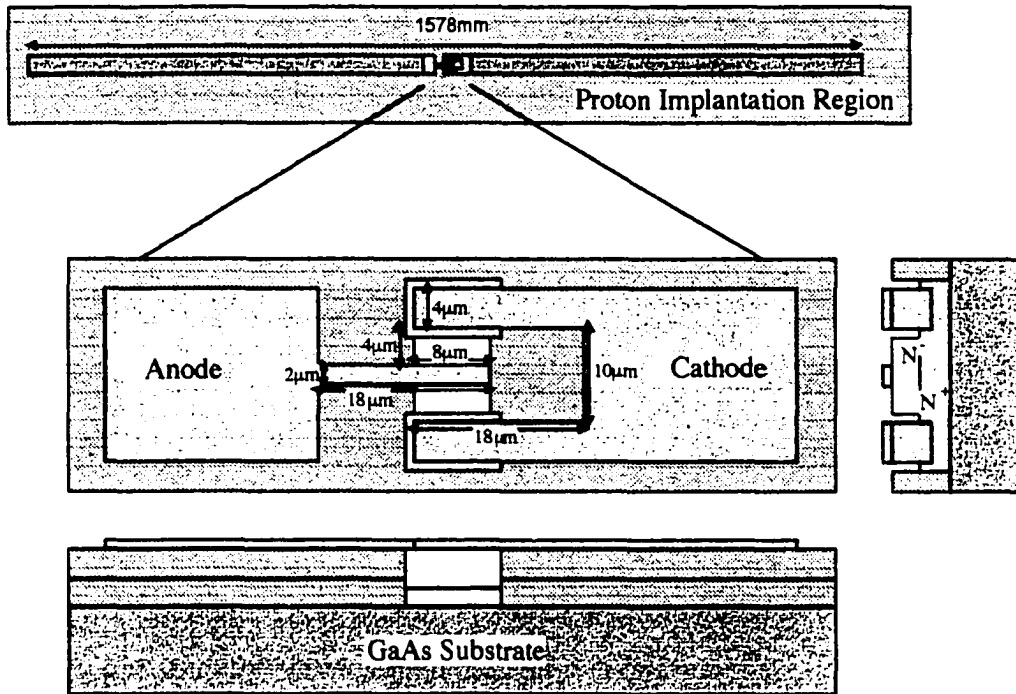
Figure 18: Dipole antenna and GaAs Schottky-diode detector

contact pads are provided by 500 Ω buried resistive lines. The resistive lines are 800 m

long and are used for low pass filtering because the contact pads each have a surface area

of 4×10^4 m^2 and act as patch antennas.

DETECTOR RESPONSE INSIDE RESONATOR

2x2 Unit Cell Resonator

To minimize the scattering loss of the GaAs substrate in the cavity, the substrate

lateral dimensions were chosen to be larger than the wavelength, 3 mm. The detectors

were fabricated on a 3-cm^2 square substrate. The substrate is polished on one side, and

etched on the other. The scattering loss of the etched side was measured and found

negligible at 100 GHz. The substrate is attached to the surface of one of the PBG mirrors

and the detector is used to measure the intensity of the electric-field standing-wave pattern

in the cavity local to the detector. Because the antenna and doped regions of the substrate

absorb radiation, the transmittance of a PBG FP cavity containing an unprocessed semi-

insulating GaAs wafer was measured first to compare the measured and modeled

transmittance. The measured transmittance is shown in Fig. 19 for both polarizations. The

simple 1-D matrix method fails to accurately predict the resonant peaks of a PBG FP

cavity with a substrate in the cavity. This failure indicates a failure of the matrix method

modeling due to perturbation of the PBG reflection phase caused by the close proximity of

the GaAs substrate to the PBG mirrors. Agreement between modeled and measured

transmittance resonance frequency is obtained (less than 5% difference) using the TMM,

which was performed by Mihail Sigalas at Ames Laboratory.

The Schottky-diode detector chosen for measurements was at the center of the

GaAs substrate and the GaAs substrate was attached to the surface a PBG mirror. The

substrate was attached to the PBG surface to ensure the substrate was parallel to the PBG
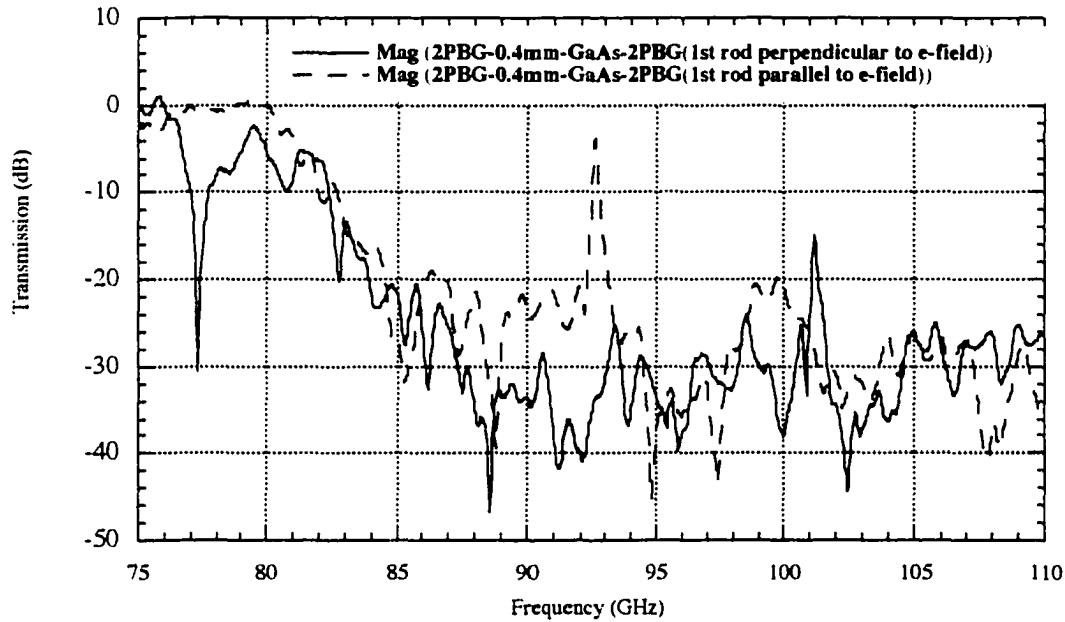
Figure 19: Measured transmittance of a W-band FP resonator with an unprocessed GaAs substrate in the cavity.

surface. The detector dipole antenna was parallel to the top layer of rods of the PBG and centered above one of the rods. The dipole antenna was centered above one of the rods to ensure that radiation scattered off the PBG is symetric in the near field. The top layer of rods on the opposing PBG mirror was perpendicular to the dipole antenna. The inner surfaces of the PBG crystals were separated by 0.9 mm, and both PBG mirrors were two unit cells thick. The transmittance and DC diode voltage response vs. frequency are simultaneously measured and the results are shown in Fig. 20. The diode has a 45 V peak

response at 94.8 GHz with a Q of 215. The transmittance shows a −18dB peak at the same frequency with a Q of 246. The transmitting horn radiates a 0.4 μW mm-wave. If the assumption is made that 100% of the radiation is incident upon the dipole antenna, a theoretical power gain of 7.4 is calculated. The low signal-to-noise ratio suggests losses present in the processed substrate.
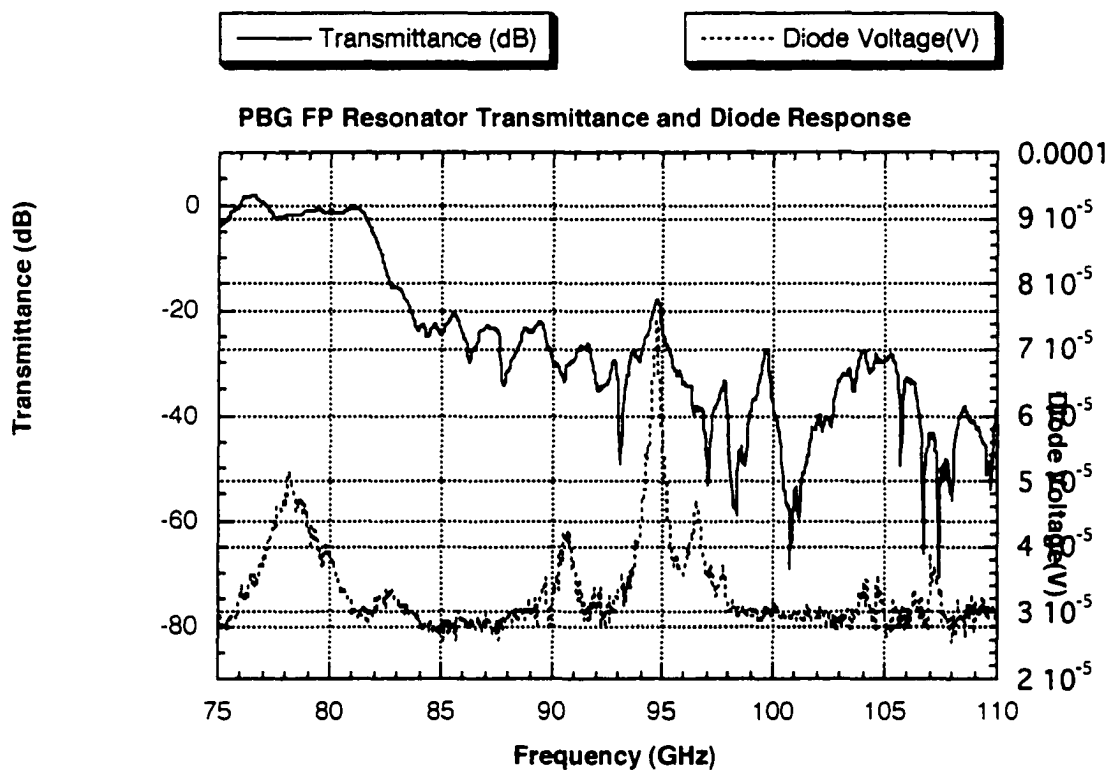
Figure 20: Transmittance and diode voltage response vs. frequency of a PBG FP resonator with a GaAs detector in the cavity. Both PBG mirrors are two unit cells thick.

2x2 Unit Cell Antenna Pattern

To measure the H-plane receiving pattern of the resonator described above, the

PBG FP resonator was rotated such that the dipole antenna in the cavity was always

parallel to the polarization vector of the incident EM wave. To measure the E-plane

receiving pattern, the dipole antenna in the cavity was perpendicular to the polarization

vector. The H-plane receiving pattern of the resonator is shown in Fig. 21. The H-plane

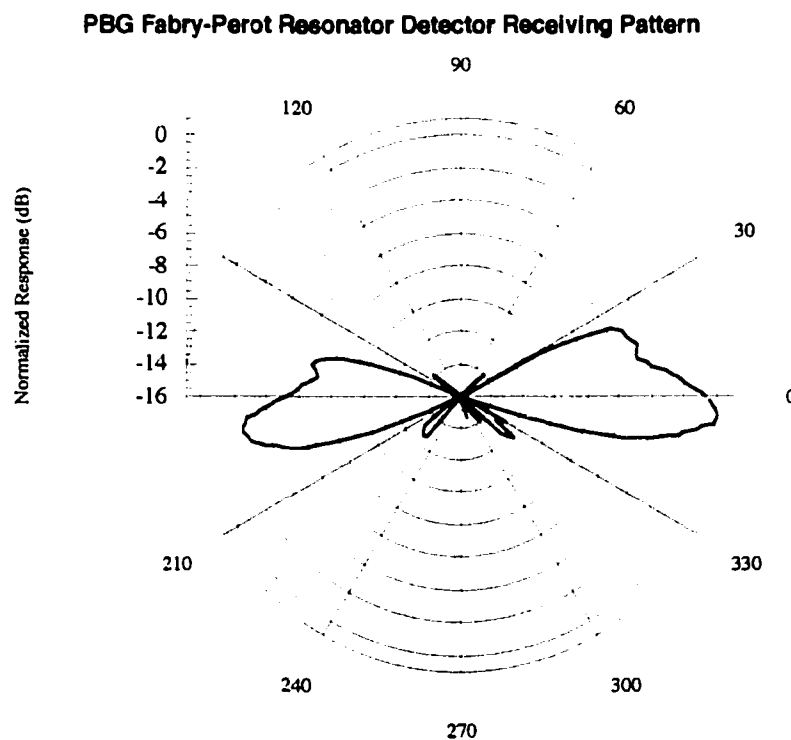pattern illustrates a maximum response at -5 degrees and a minimum half-power

Figure 21: 2x2 unit cell PBG FP resonator antenna pattern measured at 94.8 GHz. The

beam width is 18 degrees.

beamwidth of 18°. The non-symetric shape of the antenna pattern can be attributed to the detector not being perfectly centered above one of the rods on the surface of the PBG structure.

1x2 Unit Cell Resonator

To approximate the magnitude of the losses present, the diode voltage response vs. frequency is measured again with the thickness of the first PBG mirror is reduced to one unit cell. The measured voltage response vs. frequency for this case is shown in Fig. 22. The diode has a 780-μV peak response at 94.7 GHz with a Q of 279. If the same assumptions of incident power are made, the theoretical minimum power gain is now calculated to be 2050.

1x2 Unit Cell Antenna Pattern

With the thickness of the mirror opposite the GaAs substrate reduced to one unit-cell, the E- and H-plane receiving patterns of the resonator detector are measured. Plots of the E- and H-plane receiving patterns are shown in figures 23 and 24 respectively. The H-plane pattern illustrates a maximum response at 5 degrees and a minimum half-power beamwidth of 18 degrees. The E-plane pattern illustrates a maximum response at 0 degrees and a minimum half-power beamwidth of 14 degrees. Side lobes at 30 degrees in the E and H-plane patterns are formed by the cavity acting as a waveguide. The frequencies of the E and H-plane side lobes are different because the reflection phase of

the crystal planes creating the resonance conditions are different. The enhancement of

the side lobes was not calculated. The magnitude of the side lobes in the E and H-plane

pattern plots are normalized relative to the primary lobe of each plot.
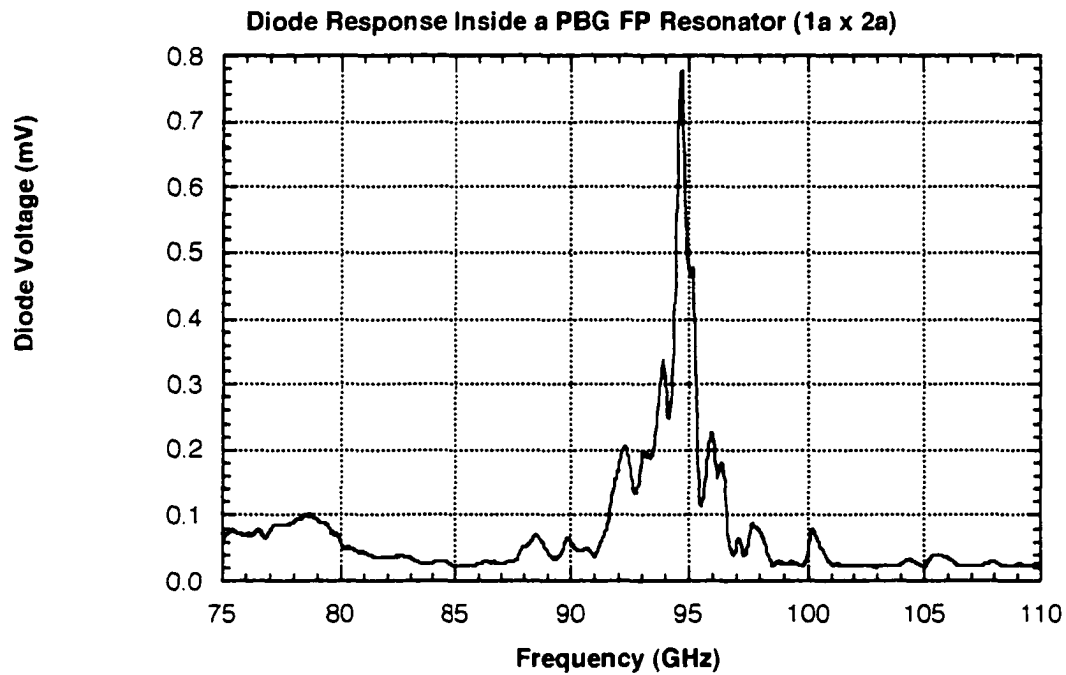
Diode Response Inside a PBG FP Resonator (1a x 2a)

Figure 22: Diode voltage response of a GaAs detector in a PBG FP resonator. The first

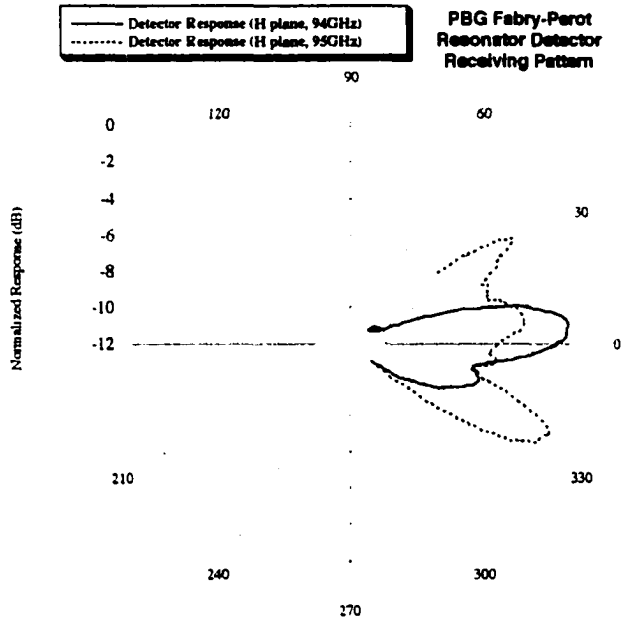PBG mirror is one unit-cell thick, and the second mirror is two unit cells thick.

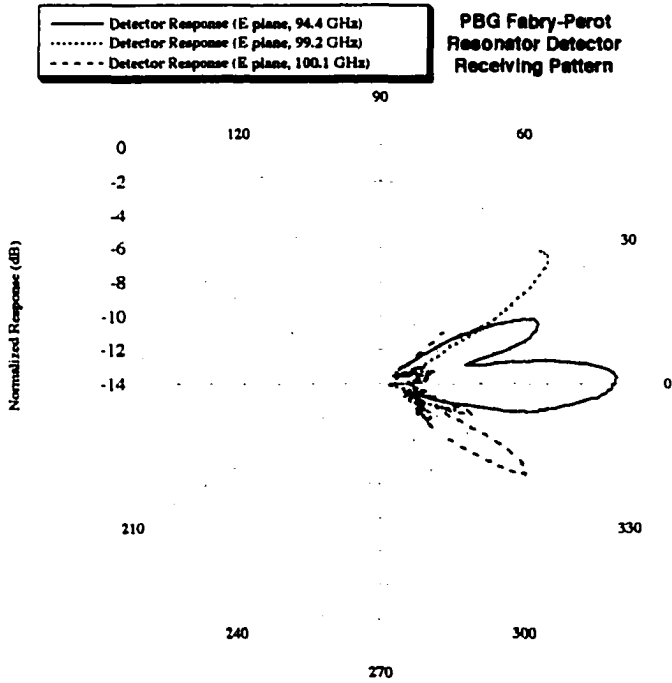Figure 23: 1x2 PBG Resonator E-Plane Antenna Pattern

Figure 24: 1x2 PBG Resonator H-Plane Antenna Pattern

PBG WAVEGUIDE INTRODUCTION

Construction

A PBG waveguide can be constructed with the three-dimensional PBG structure by removing a single rod from the center of the structure, as shown in Fig. 25. Removing a rod, creates an air cavity waveguide with a cross section 19 mm x 3 mm.

Waveguide Transmission

The transmittance of the PBG waveguide can be measured by placing transmitting and receiving horns on either end of the waveguide. The E-field polarization of the radiation is parallel to the rod stacking direction (vertical in Fig. 25). The transmittance is shown in Fig. 26 along with the transmittance of the X-Ku band PBG structure measured perpendicular to the rod stacking direction. The transmittance of the PBG waveguide is also
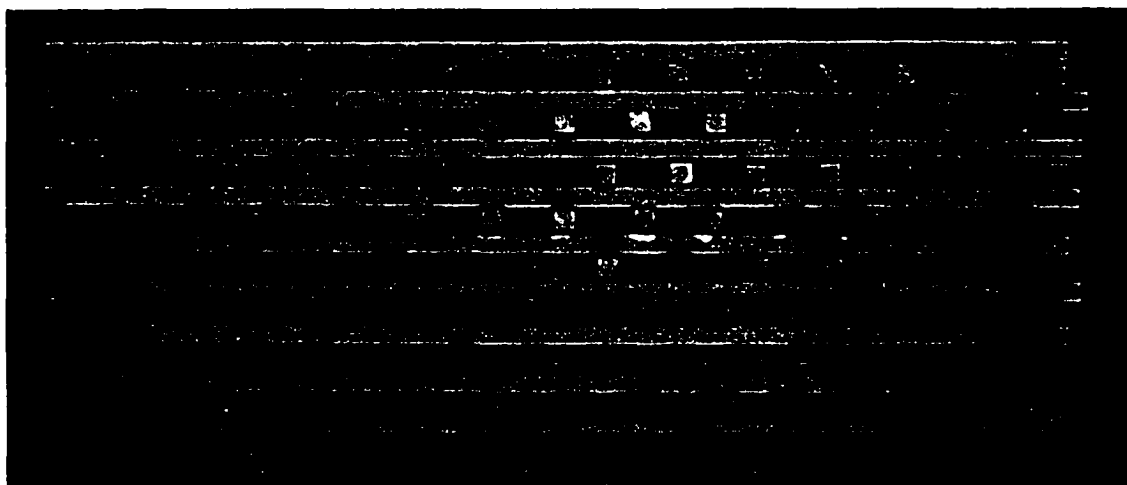

Figure 25: The X-Ku-Band PBG waveguide structure is formed by removing a rod from the structure.

shown in Fig. 27 along with the transmittance of a metal waveguide. The PBG waveguide

has a band-pass region as opposed to the high-pass region exhibited by the metal waveguide.

The upper band-edge of the PBG waveguide transmittance, not present in a metal waveguide,

is due to the variation of the PBG reflection phase with frequency. The changing reflection

phase changes the effective skin depth of the PBG structure, which in turn, changes the

waveguide cross-section. The PBG band-edges seen in Fig. 7 are for radiation travelling
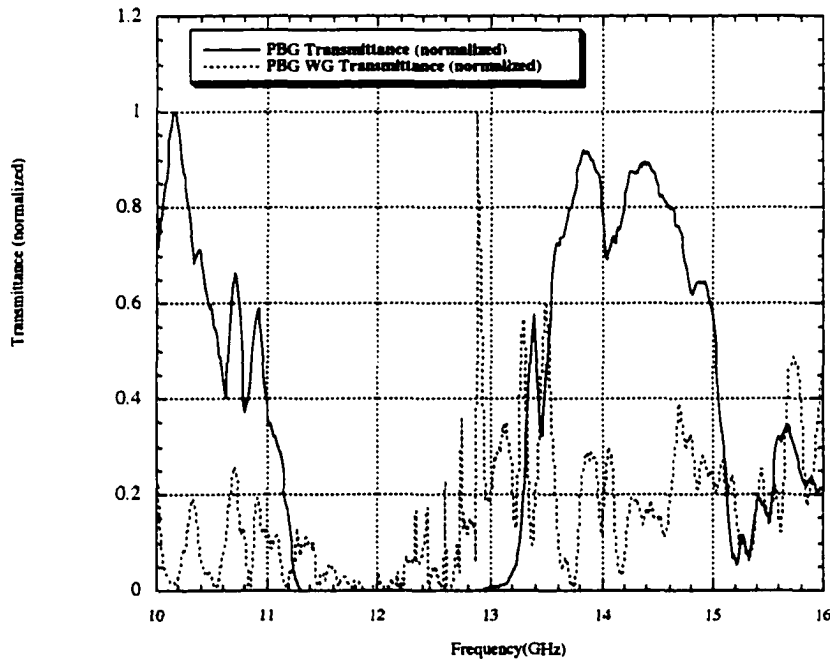

Figure 26: Measured transmittance of an X-Ku-band PBG structure and waveguide. The

transmittance is measured perpendicular to the rod stacking direction.

through the X-Ku-band PBG in the rod stacking direction. However, in the PBG waveguide, radiation is travelling perpendicular to the rod stacking direction. The PBG band-edges for radiation travelling perpendicular to the rod stacking direction can be seen in Fig. 26.

Before experimenting with different applications for the PBG waveguide, we need to determine the most effective method for coupling waves into and out of the PBG waveguide. To do this, the properties of the waveguide, such as waveguide impedance, waveguide wavelength, etc. must be measured or calculated from modeling equations.

To calculate the PBG waveguide properties using conventional metal waveguide equations, a
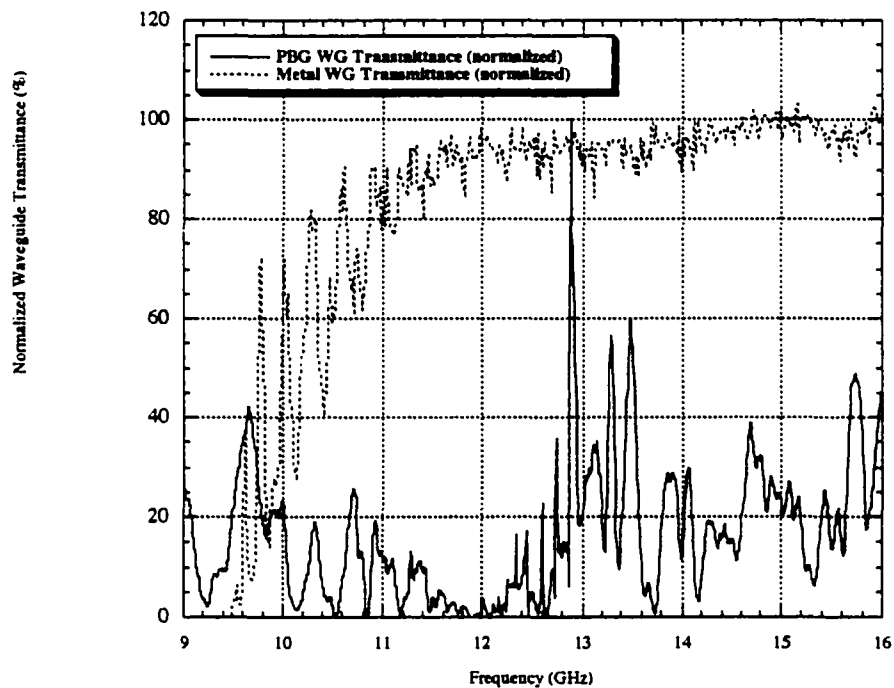

Figure 27: Measured transmittance of an X-Ku-band PBG waveguide and a metal waveguide.

modification of the metal waveguide model must be developed. We start with the metal

waveguide modeling equations given in Appendix B. The rest of the waveguide section will

be devoted to determining the properties of the PBG waveguide. Finally, we will discuss

transmittance through a 90° bend in the PBG waveguide.

Resonance Effects

The first PBG modeling issue to be investigated is the narrow waveguide

transmittance seen in figures 26 and 27. To determine if the transmittance peak represents

the full bandwidth of the PBG waveguide, or if it represents a single resonant mode created

by the confinement of waves inside the waveguide, the following measurement was devised.

A dipole antenna was inserted into the PBG waveguide as shown in Fig. 28. A tapered rod

antenna was placed in the waveguide opening as shown in Fig. 29, and a horn antenna was

placed facing the rod antenna at the edge of the rod antenna. The tapered rod antenna is used

to reduce the diffraction of radiation exiting the waveguide in order to increase the power

received by the horn antenna. Without knowing the PBG waveguide impedance, the tapered

rod antenna could not be designed for optimal coupling between the waveguide and air.

A tapered rod antenna is a dielectric rod waveguide with the lateral dimensions of the

rod tapered linearly along the lengthwise axis of the rod. A bounded wave travelling through

the dielectric rod waveguide is gradually transformed into a free space wave when the wave

encounters the taper in the waveguide. The beam width of the wave launched into free space

is reduced by making the taper more shallow and reducing the lateral dimensions of the

antenna tip. The lateral dimensions of the antenna tip must be small enough to produce a

waveguide impedance at the tip less then 377 Ω, the impedance of free space.
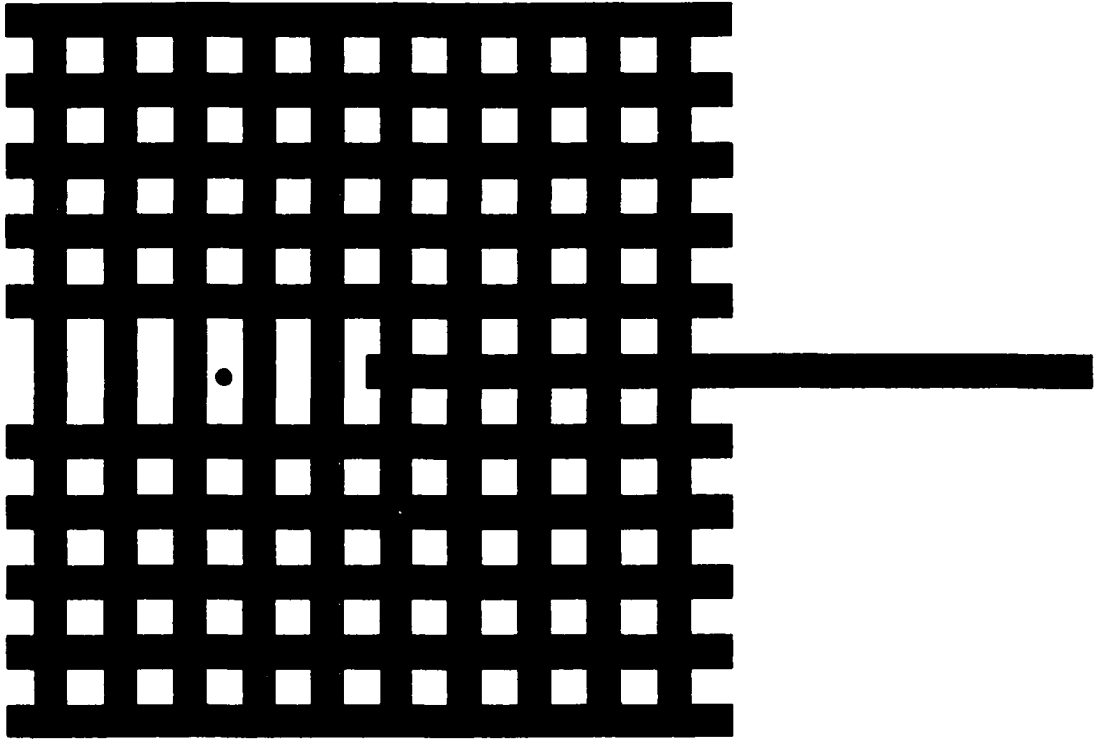
Figure 28: A dipole antenna (represented by the black dot) placed inside a PBG waveguide with a single rod placed in the waveguide to change the length of the waveguide.

The dipole antenna and a horn antenna were connected to the HP8510 network analyzer to measure the transmittance, with the dipole antenna used as the source antenna. An alumina rod is inserted into the end of the PBG waveguide and is used to vary the length of the waveguide. If the transmittance peak in figures 26 and 27 is a resonant peak, then changing the waveguide length should shift the frequency of the peak.

The alumina rod was used to vary the length of the waveguide from 9.75 cm to 12.75 cm in 0.2 mm steps. The measured transmittance of all the cavity lengths are shown in Fig. 30. Notice that three prominent resonant frequencies exist, and one is the same as the
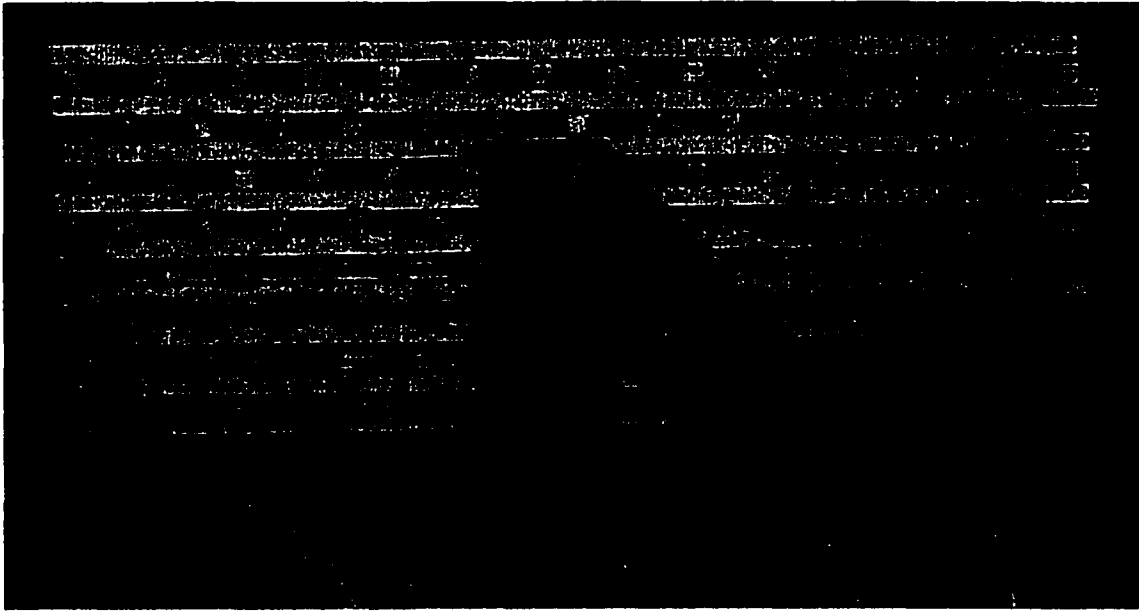
Figure 29: Tapered-rod antenna inserted into a PBG waveguide.

resonant frequency shown in figures 26 and 27. Through measurements, it was discovered

that moving the dipole antenna causes a shift in frequencies but changing the waveguide

length does not. The difference in frequency peaks between figures 26, 27, and 30 can be

attributed to the field perturbation caused by the dipole antenna. The transmittance in figures

26 and 27 was measured using two horn antennas at the ends of the PBG waveguide.

The transmittance peaks in figures 26, 27 and 30 therefore represent the transmittance

spectra of the PBG waveguide. This does not rule out the existence of resonance effects

within the PBG waveguide. Using the data from Fig. 30, the PBG waveguide transmittances

at 12.03 GHz, 12.25 GHz, and 12.72 GHz are plotted as functions of waveguide length in

Fig. 30. The variation of the transmittance indicates that there are resonance effects in the

waveguide. Figure 31 will be used again on page 52 to investigate the waveguide
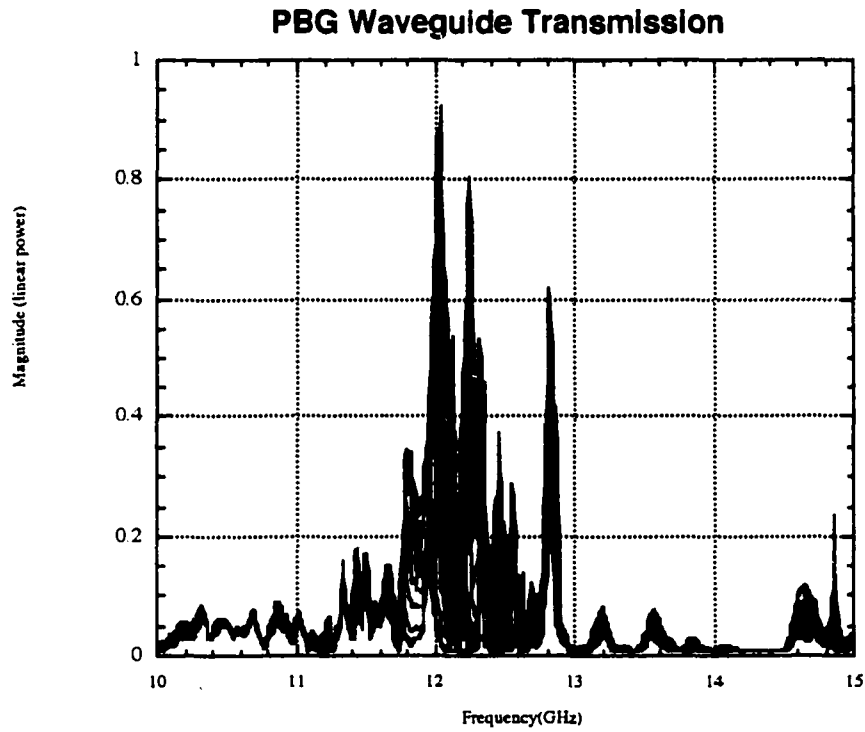
wavelength.

Figure 30: Measured transmittance of the PBG waveguide with the waveguide length varied from 9.75 to 12.75 cm.
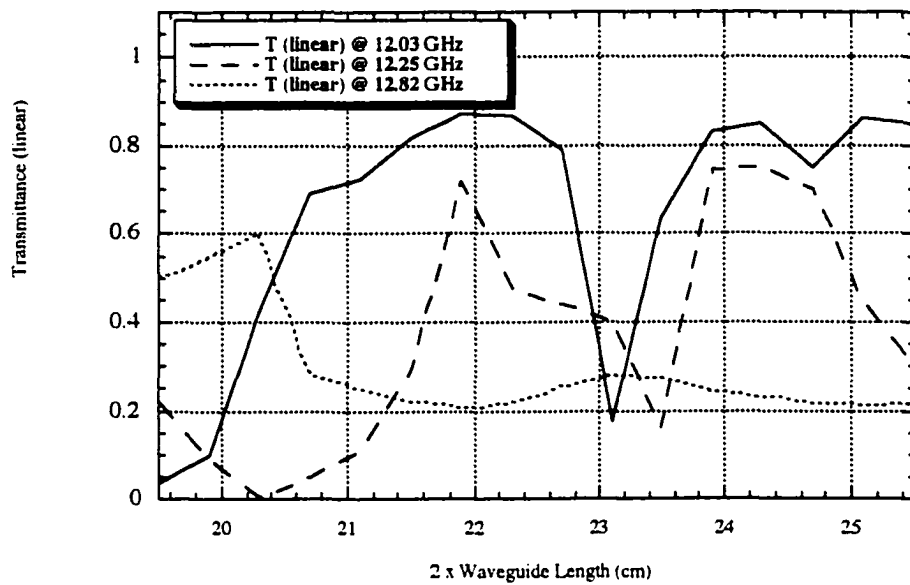
Figure 31: PBG waveguide transmittance versus waveguide length measured at 12.03 GHz,

12.25 GHz, and 12.82 GHz.

WAVEGUIDE MODES

Metal Waveguide Model

The next modeling issue to be investigated is determining which electromagnetic wave modes can exist in the waveguide. Referring to the equations in Appendix B, if the waves travelling through the waveguide are linearly polarized, then only the TE^z_{m0} modes can exist. As verification, a transmittance peak could not be found when the transmittance of the waveguide was measured with the e-field horizontally polarized in Fig. 25. This indicates that $\beta_y = 0$ as discussed in Appendix B, and only the TE^z_{m0} modes exist.

Now that it is known only the TE^z_{m0} modes exist, the next step is to determine which of the TE^z_{m0} modes are allowed within the PBG waveguide. To simplify this task, we can determine a way of modifying the modeling equations of a metal waveguide to enable us to use the equations to model a PBG waveguide. James Maloney, et. al. successfully modeled the transmittance of a waveguide constructed with a two-dimensional PBG structure using rectangular metal waveguide modeling equations [19].

Appendix B reviews the modeling of a single wave traveling through a metal waveguide as two plane waves, 180° out of phase, as shown in Fig. B1. The plane waves that reflect off the walls as they propagate down the metal waveguide and the sum of the two waves, represent the single wave propagating through the waveguide. In order to use this model with the PBG waveguide, we must change how the reflections off the waveguide walls are modeled.

Skin Depth

Electromagnetic waves reflecting off a metal do not reflect directly off the surface of a material. Instead, the reflection is distributed through a thin layer at the surface of the metal. The thin layer has a thickness less than 5 times the skin depth. However, the skin depth of a metal is thin enough to allow the approximation that reflections occur at the metal surface. A PBG, however, has a large "effective" skin depth, which prevents the assumption that reflections occur at the surface. The reflection phase of a metal can be approximated as constant and equal to either 180° or 0° as shown in Appendix B.

The wave reflection off a PBG structure is distributed over several lattice contents below the surface of the PBG structure. To enable the use of metal waveguide modeling equations, the reflection off a PBG structure can be approximated as a reflection off an imaginary plane located at a depth "d" below the surface of the PBG. The plane will be treated as having a reflection phase ϕ. Maloney, et. al. used the Finite-Difference-Time-Domain (FDTD) numerical method to calculate d and ϕ as functions of frequency and angle. Figure 32 illustrates the differences in the plane wave modeling between a metal waveguide and a PBG waveguide [20].

Without knowing d or ϕ, we can not use the waveguide modeling equations to determine which of the TE_{m0}^z modes exist. Unfortunately, the only direct measurement of PBG reflection phase available is the measure of the reflection phase relative to the PBG surface. Measuring reflection phase relative to the surface was satisfactory in modeling the one-dimensional resonators, because all measurements were performed normally incident to the PBG surface. From Fig. 32, we see that the calculation of the waveguide wavelength
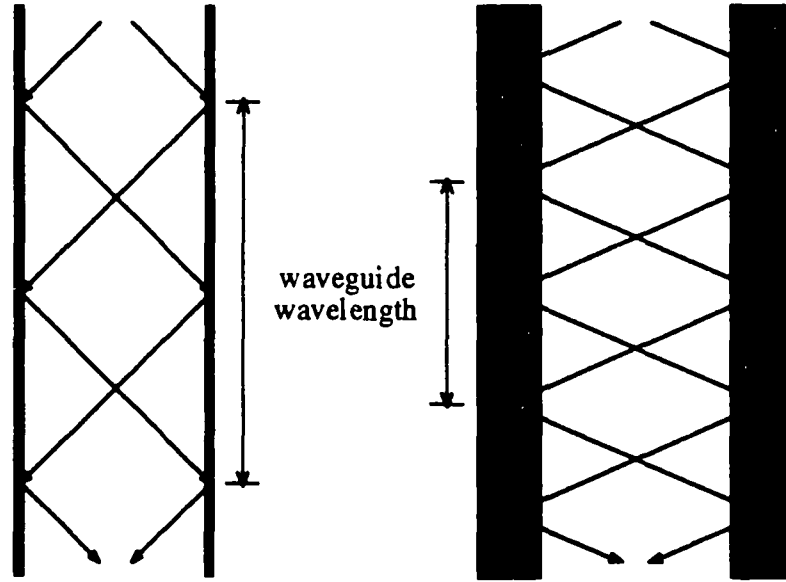
Figure 32: Plane wave models of a metal waveguide (left) and a PBG waveguide (right).

depends on knowing d and ϕ. The relation between the measured reflection phase, $\phi_{surface}$, and the modeling variables ϕ and d is given by

$$\phi_{surface}(\theta) = 4\pi \frac{d(\theta,\lambda)}{\lambda \cos(\theta)} + \phi(\theta,\lambda).$$

(11)

To overcome the problem of not knowing d and ϕ, a method was devised to extract the waveguide wavelength, λ_g, from the data in Fig. 31. The waveguide wavelength is related to d through equations 12 and 13. The angle, θ, is the reflection angle of the two waves used in the plane wave waveguide model. The wavelength, λ, is the radiation wavelength, and l is the width of the waveguide cavity.

$$\theta = \cos^{-1}\left(\frac{\lambda}{\lambda_{wg}}\right)$$

(12)

$$d = \left[\frac{\lambda}{4\sin(\theta)} - \frac{l}{2} \right] \qquad (13)$$

The method used to extract the waveguide wavelength from the transmittance vs. waveguide length data in Fig. 31 is similar to a method used by P. L. Swart et. al. to extract epi-layer thickness(es) from Transmittance vs. wavelength data [21]. Swart et. al. first transformed the Transmittance vs. wavelength data into Transmittance vs. the inverse of the wavelength data. The new data set is processed through a Fast Fourier Transform (FFT), to form a transmittance vs. resonant length data set. The maxima in this new data set are twice the optical thickness (refractive index * layer thickness) of the layer(s) in the structure under measurement. The method used is an inverse transform of the method used by Aizenberg et. al. The data in Fig. 31 is processed through a fast fourier transform algorithm. The maxima in the resulting data set are equal to the inverse of the resonant wavelength. This FFT data is transformed into FFT vs. resonant-wavelength data and plotted in Fig. 33. The waveguide wavelength is equal to the resonant wave-lengths in Fig. 33. The waveguide wavelength is always greater than the wavelength of the wave traveling through the waveguide. The wavelengths associated with 12.03 GHz, 12.25 GHz, and 12.82 GHz are 2.49 cm, 2.45 cm, and 2.34 cm respectively. From the maxima in Fig. 32, the waveguide wavelength for 12.03 is between 2.6 cm and 4.8cm. The waveguide wavelength for 12.25 GHz is greater than 3.2 cm, and the waveguide wavelength for 12.82 GHz is between 3.2 cm and 6.4 cm.

The waveguide wavelength for 12.03 GHz will be used from this point forward because its maxima is the most prominent of the three. Now that the waveguide wavelength
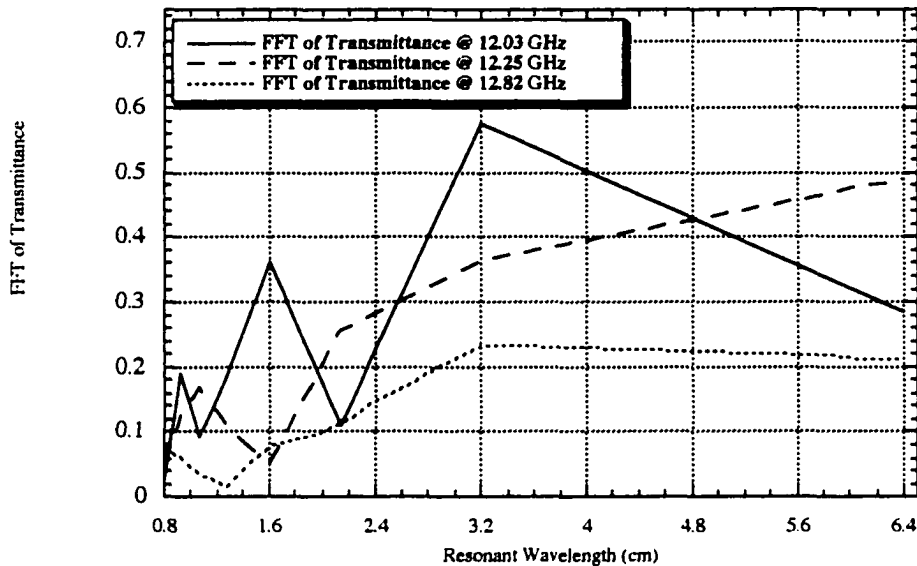
Figure 33: Fast Fourier Transform (FFT) of transmittance data in Fig. 31. Maxima in the FFT curve correspond to resonant wavelengths.

is measured, the next step is to measure the reflection phase relative to the PBG surface as a function of frequency and angle. The measurement setup used is shown in Fig. 34.

Reflection Phase

The reflection phase vs. frequency of the PBG (001) crystal planes parallel to the stacking direction were measured as several angles. The resulting data was used to produce a plot of reflection phase vs. angle for 12.06 GHz, 12.27 GHz, and 12.82 GHz as shown in Fig. 35.

Figure 34: Measurement setup used to measure reflection phase as a function of frequency and angle.

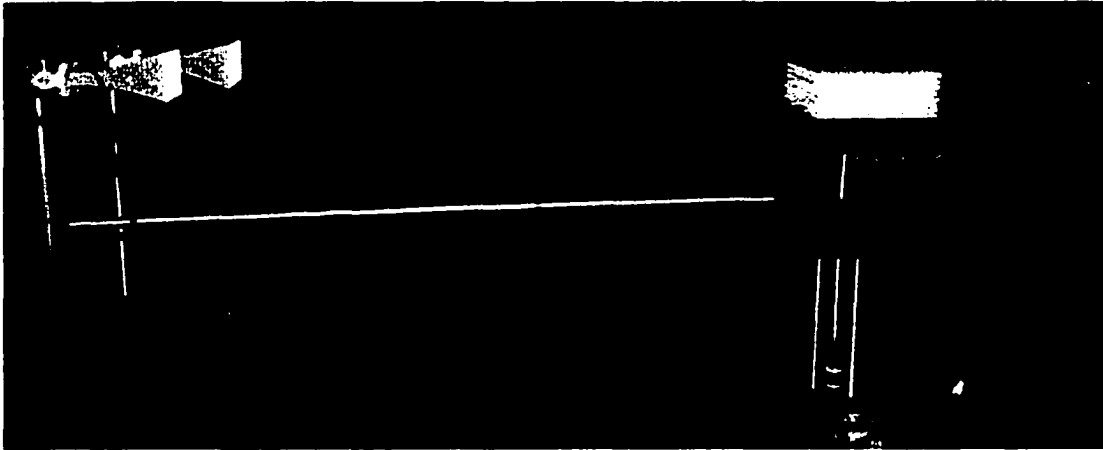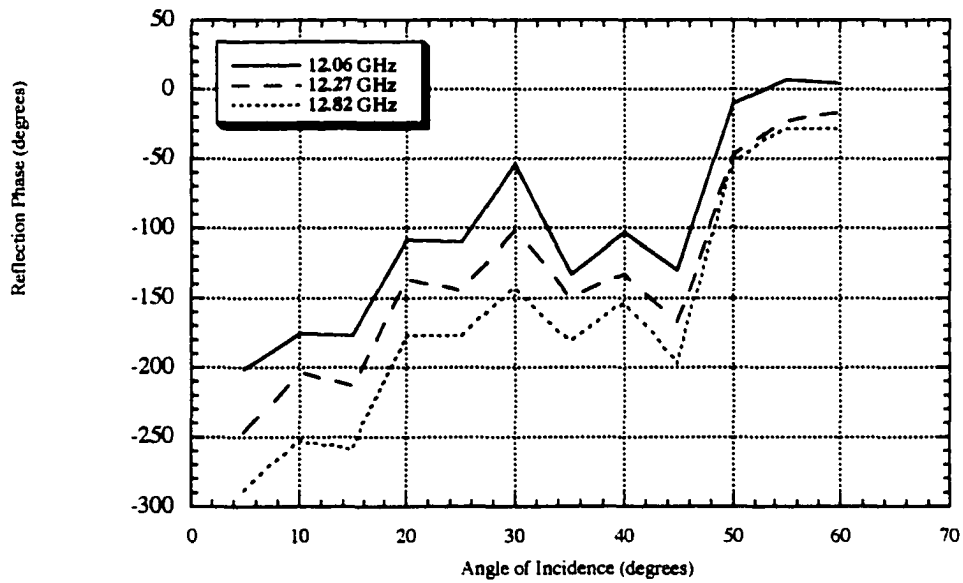Figure 35: Measured reflection phase vs. angle at the surface of the 001 crystal planes parallel to the rod stacking direction.

Using the waveguide wavelength and the measured reflection phase relative to the PBG surface, we can calculate d and ϕ at the waveguide peak transmittance frequency.

The waveguide wavelength data for 12.03 GHz allows us to calculate the reflection angle of the modeling waves in the PBG waveguide (equation 14). For 12.03 GHz, $\lambda = 2.49$ cm, and λ_{wg} is between 2.6 cm and 4.8 cm. The reflection angle, θ, is calculated to be between 17° and 59°. The waveguide wavelength also enables us to calculate d from equation 13. The depth of the reflection plane, d, is calculated to be between 0 cm and 1.179 cm. Without improving the accuracy of the calculated values for d, we cannot use the reflection phase vs. frequency data in Fig. 35 to calculate ϕ. To improve the accuracy of the calculations, the length of the PBG waveguide must be increased. The waveguide wavelength range calculated above does allow us to calculate a range of values for the cut-off frequency and waveguide impedance.

90° Waveguide Bend

A 90° bend in a PBG waveguide has a theoretical maximum transmittance of 100% by the coupling of radiation traveling down one waveguide into a second waveguide perpendicular to the first. The bend is formed by partially removing two neighboring perpendicular rods as shown in Fig. 36. Mihail Sigalas, at Ames Laboratory, theorized an optimal position and separation of these two rods relative to the intersection point of the waveguides needed for 100% transmittance. Maximum transmittance was verified for the theorized rod positioning as shown in Fig. 37. However, without proper coupling at the PBG waveguide to air transitions, 100% transmittance could not be verified. Proper coupling can not be achieved until the waveguide impedance is accurately measured or calculated.
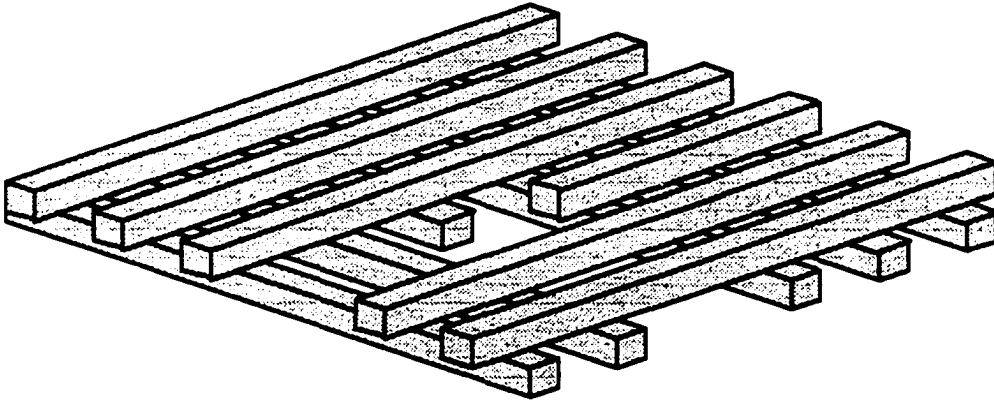
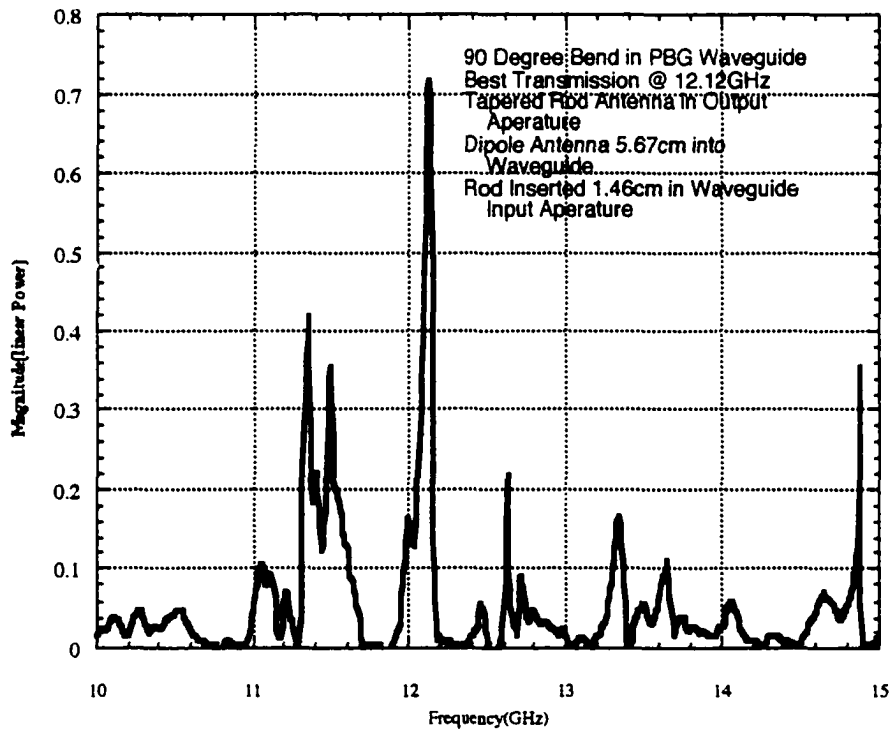Figure 36: Rod removal needed to form 90° bend in PBG waveguide.

Figure 37: Maximum transmittance measured for 90° bend in waveguide.

CONCLUSION

Fabry-Perot Resonators

In conclusion, the measured Quality factor of the W-band PBG FP resonator with a semi-insulating substrate in the cavity indicates that the photonic crystal resonator is a potential replacement to similar sized parabolic dish and optical lens antennas. Three-inch diameter optical lens antennas have gains on the order of 36dB [22]. The challenge in maximizing the gain enhancement of the PBG FP resonator is in reducing the effects of loss in the detectors, which are inserted into the cavity. Although the embedded detectors presented in this paper have low gains due to high losses in the detector substrate, the 18 degree beam width and the low quality factor enables the resonator to be used to enhance the performance of optical lens antennas. This would be accomplished by placing the resonator at the focus point of the lens.

The difference in resonant transmission peak amplitudes and Q factor values between the resonators with semi-insulating and processed substrates suggests a high loss inside the cavity due to the processed surface of the substrate. The asymmetric shape of the PBG FP resonator detector receiving patterns suggests the asymmetric placement of the dipole antenna in the cavity, relative to the rods.

PBG Waveguides

In order to use PBG waveguides as a cost effective replacement to metal waveguides, the transmittance effeciency of the waveguides must be maximized by optimizing the coupling between PBG waveguides and other waveguides or air. The resonance effects found within the waveguide are evidence of the coupling problem. To optimize the waveguide

efficiency, the PBG waveguide impedance must accurately measured or calculated. A method for measuring the PBG waveguide wavelength which can be used to calculate the waveguide impedance was shown, but its successful use is dependant upon having a PBG waveguide of adequate length. Once the waveguide impedance is found, a tapered rod antenna can be designed to optimally couple the PBG waveguide to other waveguides and air.

ACKNOWLEGEMENTS

APPENDIX A. RESONATOR THEORY

An electromagnetic plane wave incident upon a single epilayer at an incident angle θ_i will reflect and transmit through the epilayer as shown in Figure A1 below.

Parallel electromagnetic rays having the same wavelength and polarization will add vectorily, allowing us to express the total reflection and transmission as an infinite series.
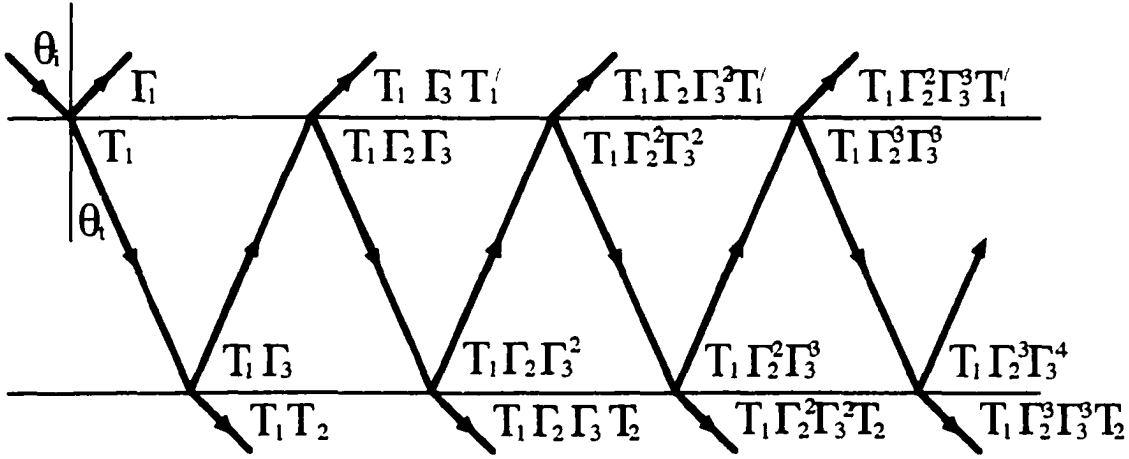
Figure A1: Illustration of the reflectance and transmittance of a thin film on a substrate.

$$n_i \sin(\theta_i) = n_t \sin(\theta_t)$$

$$\delta_i = \frac{2\pi}{\lambda} n_i d_i \cos(\theta_i)$$

$$r = \Gamma_1 + T_1\Gamma_3 T_1' \exp(-j2\delta) + T_1\Gamma_2\Gamma_3^2 T_1' \exp(-j4\delta) + ...$$

$$= \Gamma_1 + \frac{T_1 T_1' \Gamma_3 \exp(-j2\delta)}{1 - \Gamma_2\Gamma_3 \exp(-j2\delta)} \tag{A1}$$

$$t = T_1 T_2 \exp(-j\delta) + T_1\Gamma_2\Gamma_3 T_2 \exp(-j3\delta) + T_1\Gamma_2^2\Gamma_3^2 T_2 \exp(-j5\delta) + ...$$

$$= \frac{T_1 T_2 \exp(-j\delta)}{1 - \Gamma_2\Gamma_3 \exp(-j2\delta)} \tag{A2}$$

The total reflection and transmission of a resonator constructed with two parallel planar

mirrors is almost identical to the total reflection of an epilayer. We can still assume that

$|\Gamma_1| = |\Gamma_2|$ and $|\Gamma_3| = |\Gamma_4|$, but we can not assume $\Gamma_1 = -\Gamma_2$ and $\Gamma_3 = -\Gamma_4$.

To simplify the equations for total reflection and transmission, the reflection and

transmission of the mirrors are written in polar form.

$$r = |\Gamma_1|\exp(-j\phi_{\Gamma_1}) + \frac{|T_1||T_1'||\Gamma_3|\exp(-j(2\delta + \phi_{\Gamma_3} + \phi_{T_1} + \phi_{T_1'}))}{1 - |\Gamma_2||\Gamma_3|\exp(-j(2\delta + \phi_{\Gamma_2} + \phi_{\Gamma_3}))} \tag{A3}$$

$$= \frac{|\Gamma_2|\exp(-j\phi_{\Gamma_1}) - |\Gamma_3|\exp(-j(2\delta + \phi_{\Gamma_3}))[|\Gamma_2|^2\exp(-j(\phi_{\Gamma_1} + \phi_{\Gamma_2})) - (1 - |\Gamma_2|^2)\exp(-j(\phi_{T_1} + \phi_{T_1'}))]}{1 - |\Gamma_2||\Gamma_3|\exp(-j(2\delta + \phi_{\Gamma_2} + \phi_{\Gamma_3}))}$$

$$t = \frac{|T_1||T_2|\exp(-j(\delta + \phi_{T_1} + \phi_{T_2}))}{1 - |\Gamma_2||\Gamma_3|\exp(-j(2\delta + \phi_{\Gamma_2} + \phi_{\Gamma_3}))} \tag{A4}$$

The resonance condition is achieved when the transmission of the resonator is

maximized. This occurs when the exponential in the denominator of equation A4 is equal to one.

The resonance condition is thus given by

$$\upsilon_{peak} = \frac{m - \frac{\phi_1 + \phi_2}{2\pi}}{2L} \cdot c \tag{A5}$$

where $\phi_1 = \phi_{\Gamma_1}$ and $\phi_2 = \phi_{\Gamma_2}$.

The electromagnetic field enhancement inside the cavity can be found by adding the

fields inside the cavity vectorily.

$$g = T_1\exp\left(-j\frac{x\delta}{d}\right) + T_1\Gamma_3\exp\left(-j\left(2\delta - \frac{x\delta}{d}\right)\right) + T_1\Gamma_2\Gamma_3\exp\left(-j\left(2\delta + \frac{x\delta}{d}\right)\right) + \dots$$

$$= \frac{|T_1|\left(\exp\left(-j\frac{x\delta}{d}\right) + |\Gamma_3|\exp\left(-j\left(\phi_{\Gamma_3} - \frac{x\delta}{d}\right)\right)\right)}{1 - |\Gamma_2||\Gamma_3|\exp\left(-j\left(2\delta + \phi_{\Gamma_2} + \phi_{\Gamma_3}\right)\right)}$$

The total reflectance and transmittance waves for a resonator with two or more epilayers within the resonator cavity can be solved numerically using a computer ray tracing program. However, ray tracing programs are slow and require large amounts of memory. An alternative to ray tracing is the matrix method. The reflective, transmissive, and absorbive propertives of a single epilayer are represented by a 2x2 matrix. The reflectance and transmittance of a structure can be found by multiplying the matrices representing the different layers together to form a single matrix. The exact equations are

$$C_m = \begin{pmatrix} \exp(j\delta_{m-1}) & \Gamma_m^b \exp(j\delta_{m-1}) \\ \Gamma_m^b \exp(-j\delta_{m-1}) & \exp(-j\delta_{m-1}) \end{pmatrix} \qquad \begin{pmatrix} a & b \\ c & d \end{pmatrix} = (C_1)(C_2)...(C_{n+1})$$

$$\sqrt{R} = \sqrt{rr^*} = \frac{cc^*}{aa^*} \qquad\qquad \sqrt{T} = \sqrt{tt^*} = \frac{(t_1 t_2 ... t_{n+1})(t_1^* t_2^* ... t_{n+1}^*)}{aa^*}$$

These equations must be modified slightly for a Fabry-Perot resonator.

APPENDIX B. WAVEGUIDE THEORY

The field configurations of an electromagnetic wave travelling through a rectangular waveguide orientated along the z-axis are either transverse magnetic (TM^z) or transverse electric (TE^z). The equations for a TM^z wave in rectangular coordinates are

$$E_x = \frac{-j}{\omega\mu\varepsilon}\frac{\partial^2 A_z}{\partial x\partial z} \qquad\qquad H_x = \frac{1}{\mu}\frac{\partial A_z}{\partial y}$$

$$E_y = \frac{-j}{\omega\mu\varepsilon}\frac{\partial^2 A_z}{\partial y\partial z} \qquad\qquad H_y = \frac{-1}{\mu}\frac{\partial A_z}{\partial x} \qquad\qquad (B.1)$$

$$E_z = \frac{-j}{\omega\mu\varepsilon}\left(\frac{\partial^2}{\partial z^2}+\beta^2\right)A_z \qquad H_z = 0$$

The equations for a TE^z wave are

$$E_x = \frac{-1}{\varepsilon}\frac{\partial F_z}{\partial y} \qquad\qquad H_x = \frac{-j}{\omega\mu\varepsilon}\frac{\partial^2 F_z}{\partial x\partial z}$$

$$E_y = \frac{1}{\varepsilon}\frac{\partial F_z}{\partial x} \qquad\qquad H_y = \frac{-j}{\omega\mu\varepsilon}\frac{\partial^2 F_z}{\partial y\partial z} \qquad\qquad (B.2)$$

$$E_z = 0 \qquad\qquad H_z = \frac{-j}{\omega\mu\varepsilon}\left(\frac{\partial^2}{\partial z^2}+\beta^2\right)F_z$$

Enforcing boundary conditions at the waveguide walls leads to the following solutions for the TE^z waves.

$$E_x^+ = A_{mn} \frac{\beta_y}{\varepsilon} \cos(\beta_x x) \sin(\beta_y y) e^{-j\beta_z z}$$

$$E_y^+ = -A_{mn} \frac{\beta_x}{\varepsilon} \sin(\beta_x x) \cos(\beta_y y) e^{-j\beta_z z}$$

$$E_z^+ = 0$$

$$H_x^+ = A_{mn} \frac{\beta_x \beta_z}{\omega\mu\varepsilon} \sin(\beta_x x) \cos(\beta_y y) e^{-j\beta_z z} \qquad\qquad (B.3)$$

$$H_y^+ = A_{mn} \frac{\beta_y \beta_z}{\omega\mu\varepsilon} \cos(\beta_x x) \sin(\beta_y y) e^{-j\beta_z z}$$

$$H_z^+ = -jA_{mn} \frac{\beta_c^2}{\omega\mu\varepsilon} \cos(\beta_x x) \cos(\beta_y y) e^{-j\beta_z z}$$

$$\beta_c^2 = \left(\frac{2\pi}{\lambda_c}\right)^2 = \beta^2 - \beta_z^2 = \beta_x^2 + \beta_y^2 = \left(\frac{m\pi}{a}\right)^2 + \left(\frac{n\pi}{b}\right)^2$$

where β_c is the cutoff wave number and $v_c = \frac{1}{\sqrt{\mu\varepsilon}\lambda_c}$ is the cutoff frequency of the

waveguide. m and n are the orders of the TE_{mn}^{+z} modes. Notice if the wave is linearly

polarized such that $E_x = 0$, then $\beta_y = 0$ and $n = 0$, the only modes allowed are TE_{m0}^{+z} modes.

The equations for the TE_{m0}^{+z} modes are

$$E_x^+ = 0 \qquad\qquad\qquad H_x^+ = A_{mn} \frac{\beta_x \beta_z}{\omega\mu\varepsilon} \sin(\beta_x x) e^{-j\beta_z z}$$

$$E_y^+ = -A_{mn} \frac{\beta_x}{\varepsilon} \sin(\beta_x x) e^{-j\beta_z z} \qquad H_y^+ = 0 \qquad\qquad (B.4)$$

$$E_z^+ = 0 \qquad\qquad\qquad H_z^+ = -jA_{mn} \frac{\beta_c^2}{\omega\mu\varepsilon} \cos(\beta_x x) e^{-j\beta_z z}$$

Enforcing the boundary conditions for the TM^z waves leads to the following

solutions.

$$E_x^+ = -B_{mn} \frac{\beta_x \beta_z}{\omega \mu \varepsilon} \cos(\beta_x x) \sin(\beta_y y) e^{-\jmath \beta_z z}$$

$$E_y^+ = -B_{mn} \frac{\beta_y \beta_z}{\omega \mu \varepsilon} \sin(\beta_x x) \cos(\beta_y y) e^{-\jmath \beta_z z}$$

$$E_z^+ = -jB_{mn} \frac{\beta_c^2}{\omega \mu \varepsilon} \sin(\beta_x x) \sin(\beta_y y) e^{-\jmath \beta_z z}$$

$$H_x^+ = B_{mn} \frac{\beta_y}{\varepsilon} \sin(\beta_x x) \cos(\beta_y y) e^{-\jmath \beta_z z} \qquad \text{(B.5)}$$

$$H_y^+ = -B_{mn} \frac{\beta_x}{\varepsilon} \cos(\beta_x x) \sin(\beta_y y) e^{-\jmath \beta_z z}$$

$$H_z^+ = 0$$

With the same condition $E_x = 0$, notice if either $\beta_x = 0$ or $\beta_y = 0$, then

$E_x^+ = E_y^+ = E_z^+ = 0$. Therefore, the TE modes are the only allowed modes when the wave is

linerly polarized.

The field equations of a linearly polarized wave travelling down a waveguide are

given by equations B.4. The electric field equation of this wave is given by equation B.6.

$$E_y^+ = -A_m \frac{\beta_x}{\varepsilon} \sin(\beta_x x) e^{-\jmath \beta_z z} \qquad \text{(B.6)}$$

By using the trigonometric identity $\sin(x) = \frac{1}{2j}\left[e^{jx} - e^{-jx}\right]$, equation B.6 can be

rewritten to form equations B.7 and B.8.

$$E_y^+ = A_m \frac{j\beta_x}{2\varepsilon}\left[e^{j(\beta_x x - \beta_z z)} - e^{-j(\beta_x x + \beta_z z)}\right] \qquad \text{(B.7)}$$

$$\beta_x = \beta \sin\psi \quad \text{and} \quad \beta_z = \beta \cos\psi$$

$$E_y^+ = A_m \frac{j\beta_x}{2\varepsilon}\left[e^{j\beta(x \sin\psi - z \cos\psi)}\right] - A_m \frac{j\beta_x}{2\varepsilon}\left[e^{-j\beta(x \sin\psi + z \cos\psi)}\right] \qquad \text{(B.8)}$$

Equation B.8 represents two waves travelling down the waveguide as shown in figure

B1. The two waves are 180° out of phase. The directions of propagation of the two waves

have equal z components, no x components, and opposite y components. The sum of the two

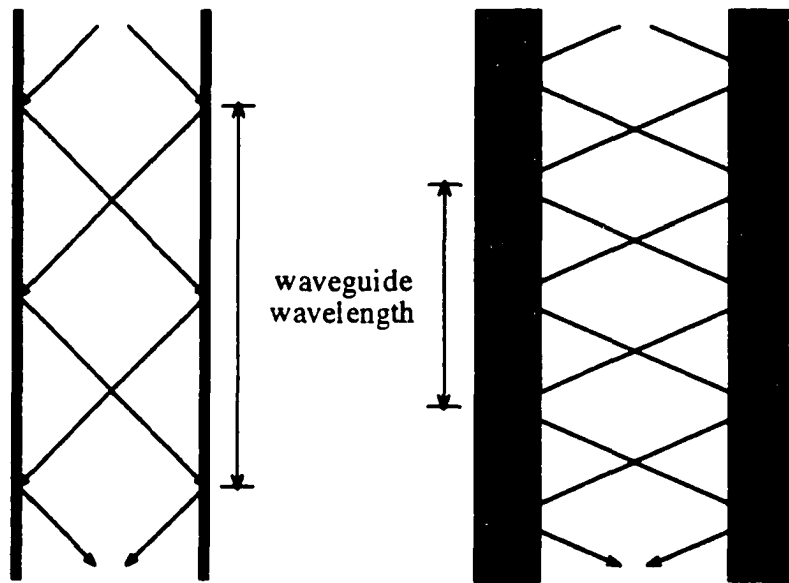waves results in a direction of propagation along the z-axis.

waveguide
wavelength

Figure B1: Metal waveguide

The cut-off frequency of a metal waveguide is given by equation 1.

$$\left(v_c\right)_{m,n} = \frac{1}{2\pi\sqrt{\mu\varepsilon}} \sqrt{\left(\frac{m\pi}{a}\right)^2 + \left(\frac{n\pi}{b}\right)^2}$$
(1)

where a and b are the cross section dimensions of the waveguide, and m and in are the order

of the waveguide modes and are none negative integers.

APPENDIX C. DETECTOR FABRICATION

The W-band power detector consists of an Aluminum Microstrip dipole antenna connected across a GaAs schottky diode with buried resistive lines connecting the anode and cathode of the diode to two gold wire bonding pads. Neighboring detectors on a substrate are isolated from one another with proton bombardment. The schottky diode process traveler was modeled after a process traveler developed at Stanford University. The process traveler is made up of five parts: MBE growth, cathode etch/metalization, proton implantation, anode metalization, and antenna metalization.

MBE Growth

The first part of the process traveler was the MBE growth, where silicon doped n- and n+ layers are grown on a semi-insolating GaAs substrate. Table C.1 lists the specifications for the three layers.

TABLE C.1

Layer	Description	Thickness	Doping Level
top	n-	$0.6\,\mu m$	$3 \cdot 10^{16} cm^{-3}$
bottom	n+	$0.8\,\mu m$	$6 \cdot 10^{18} cm^{-3}$
substrate	semi-insulating	$500\,\mu m$	intrinsic

Cathode Etch/Metalization

The second part of the process traveler was the cathode etch/metalization. In this step, wells are etched through the n- layer, and ohmic contacts are deposited in the wells. Each detector will have six ohmic contacts. Two will act as cathode contacts, and the other

four will act as buried resistor contacts. The etch process consists of three steps: photolithography, wet etch, and metalization/lift-off.

In the photolithography step, the substrate is first placed in a 120°C oven for 30 minutes to dehydrate the surface of the substrate. The substrate is then placed on a spinner and HMDS Adhesion promoter is spun on the substrate. Next, a layer of positive photoresist (AZ5209E) approximately $1.7 \mu m$ thick is spun on the substrate. The substrate is then placed in a 85°C oven for 30 minutes to soft bake the photoresist. Using a Karl Suss mask aligner and the mask pattern shown in figure C.1, the photoresist is exposed for 50-60 seconds. The photoresist is developed and then post baked for at least 40 minutes in a 120°C oven to harden the photoresist. A profilometer is then used to measure the photoresist thickness. The two sets of lengths shown in figure C.1 correspond to two different sizes of Schottky diodes fabricated.
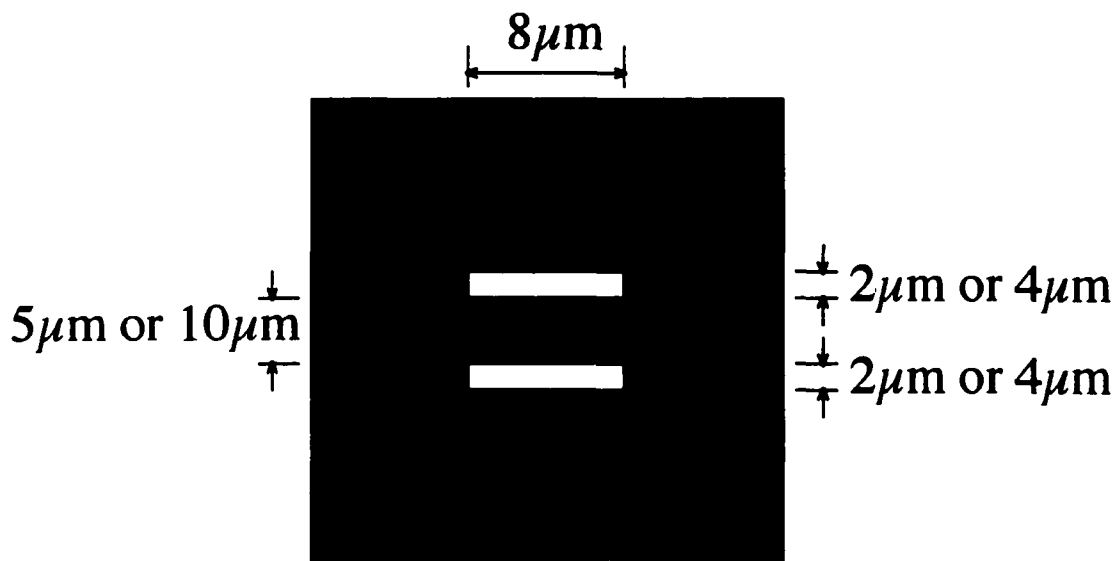
Figure C.1: Mask 1

The wet etch step is performed by first mixing a GaAs etch solution and diluting with De-ionized (DI) water to slow the etch rate. The etch solution $NH_4OH : H_2O_2 : H_2O$ (70:12:1000) is mixed in a teflon beaker and the beaker is placed in a large water bath which is used to maintain a constant temperature over time. A test wafer is etched for one minute and rinsed with DI water for two minutes to stop the etch. A profilometer is then used to measure the etch depth and an etching rate is calculated. The etch rate for the solution listed is typically 0.3-0.6 μm/minute. Etch times are chosen to produce an etch depth of 0.75μm. A profilometer is used to verify the etch depths.

The metalization/lift-off step is performed by first etching the wafer for 60 seconds in a Buffered Oxide Etch. The wafer is then placed in an e-beam metalization chamber and the wafer is metalized with the metals listed in table C.2.

Table C.2

Metal	Thickness	Deposition sequence
Ge (Germanium)	108 Å	1st deposition
Au (Gold)	102 Å	2nd deposition
Ge	63 Å	3rd deposition
Au	236 Å	4th deposition
Ni (Nickle)	100 Å	5th deposition
Au	7200 Å	6th deposition

After metalization, the sample is soaked in acetone to breakdown the photoresist and lift-off the metal. A cross-section of the sample after completion of the cathode etch/metalization is shown in figure C.2.

Proton Implantation

The third part of the process traveler is the proton implantation. In this part, a barrier

layer is deposited and patterned on the sample, and a proton implantation process is used to

electrically isolate neighboring detectors from one another. The proton implantation process

consists of six steps: spin-on glass, metalization, photolithography, pan etch, proton
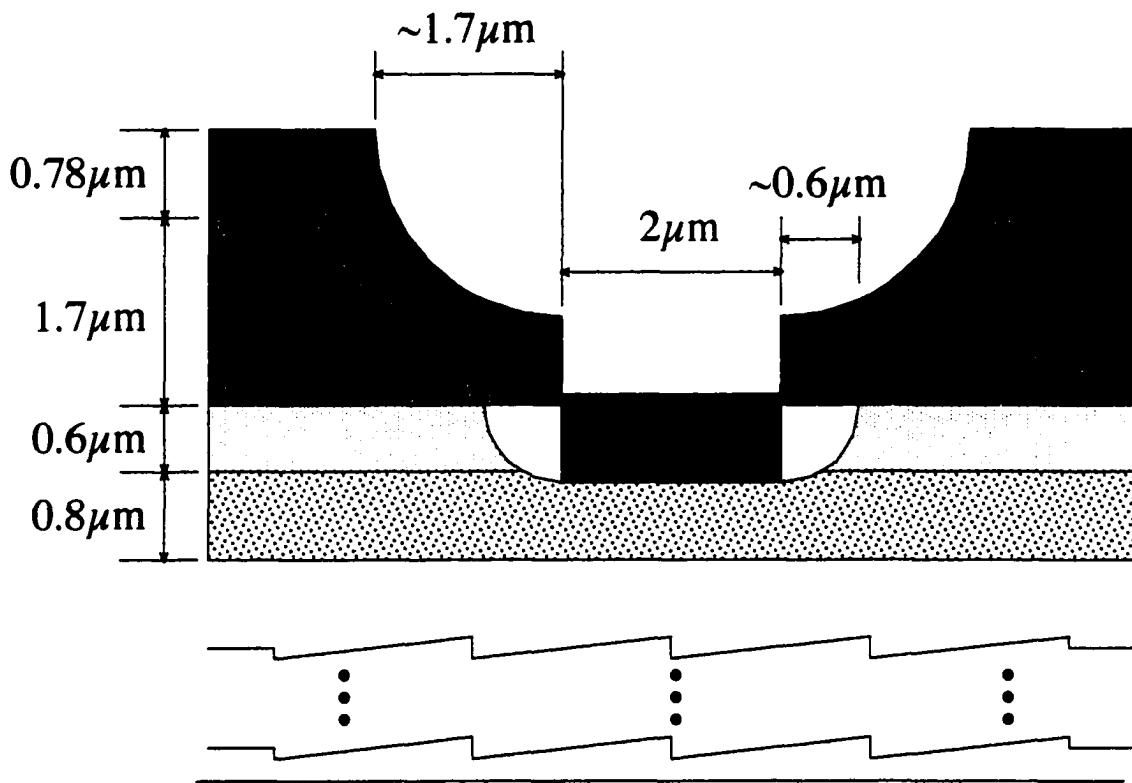
implantation, and spin-on glass/metal removal.

Figure C.2: Process 1

In the spin-on glass step, a $0.2\mu m$ layer of Accuglass 512 is spun on the substrate and

is baked at 400°C for one hour in a nitrogen ambient. After baking, Accuglass 512 can be

etched with silicon dioxide etches such as BOE. In the metalization step, an e-beam

metalization chamber is used to deposit a $1.7\mu m$ layer of aluminum over the spin-on glass layer.

The photolithography step is identical to the previously described photolithography step, except the photoresist layer is $1.1\mu m$ thick and the mask used in this step is shown in figure C.3. The photolithography step leaves rectangular patches of photoresist covering what will be the buried resistor lines and diode active regions.
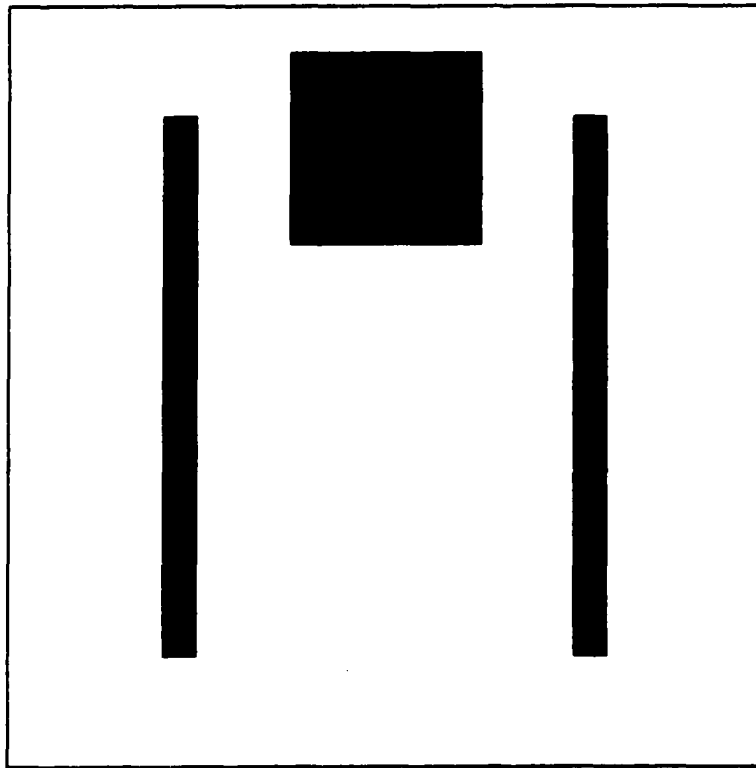

Figure C.3: Mask 2

In the pan-etch step, the fast pan etch solution $CH_3COOH : H_3PO_4 : HNO_3 : H_2O$ (1:16:1:2) is mixed. The samples are placed in the solution to etch through the Aluminum layer. Without agitation, the etch required between 20 to 60 minutes. The samples are then

rinsed in DI water for two minutes to stop the etch. The samples are then soaked in acetone, methenol, and then DI water to remove the photoresist. A BOE etch is then performed to etch through the spin-on glass layer, leaving an aluminum on spin-on glass mesa. Figure C.4 shows a cross-section of the sample after etching.
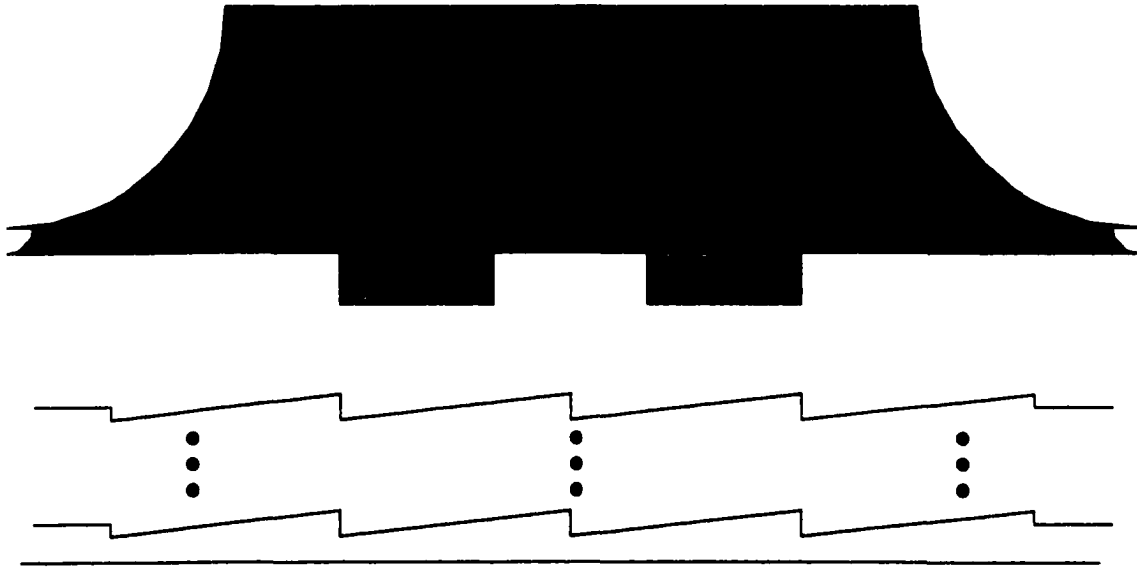

Figure C.4: Process 2

The sample is then sent out for proton (Hydrogen) implantation. The following dosages were used to compensate for the $6 \cdot 10^{18} cm^{-3}$ and $3 \cdot 10^{16} cm^{-3}$ Silicon doping levels in the two MBE grown layers.

$1 \cdot 10^{15} cm^{-3}$ at $110 keV$

$2 \cdot 10^{15} cm^{-3}$ at $190 keV$

After proton implantation, the sample is placed in a BOE etch to remove the remaining spin-on glass and lift-off the remaining metal.

Anode Metalization

The fourth part of the process traveller was the anode metalization. In this part, the

final anode and cathode contacts and the detector wire bonding pads are deposited and

patterned on the sample. The anode metalization consists of three steps: BOE etch,

photolithography, and metalization/lift-off.

In the BOE etch, the sample is placed in BOE for 60 seconds to remove any residual

spin-on glass on the sample surface. The photolithography step is identical to the

photolithography step described in the Cathode etch/metalization, except the photoresist is

$1.1\mu m$ thick, the sample is soaked in Chlorobenzene for 10 minutes immediately prior to

developing, and there is no post bake after developing the photoresist. The mask pattern

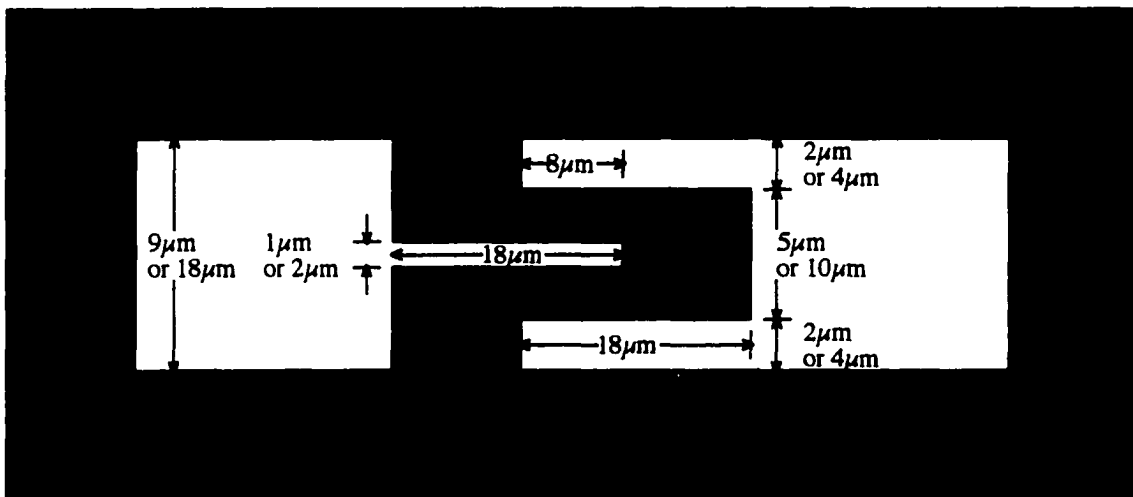used in the photolithography step is shown in figure C.5.

Figure C.5: Mask 3

In the metalization/lift-off, a 500Å layer of Titanium and a 2500Å layer of Gold were deposited using e-beam metalization. Acetone was then used to remove the photo-resist and lift-off the metal.

Antenna Metalization

The final step in the process traveller was the dipole antenna metalization. In this step, an Aluminum dipole antenna is patterned on the diode contacts and the detector fabrication is completed. The antenna metalization consists of two steps: photolithography and metalization/lift-off. The photolithography step is identical to the one used in the Anode metalization step. In the metalization/lift-off step, a 6000Å layer of Aluminum is deposited using e-beam metalization. Acetone was then used to remove the photo-resist and lift-off the metal.

Approximately one dozen detectors were separated the from the wafer by using a wafer scriber and a wafer breaker. The remaining detectors were kept on a single substrate.

REFERENCES

[1] K. M. Ho, C. T. Chan, and C. M. Soukoulis, "Existance of a Photonic Gap in Periodic Dielectric Structures," Physical Review Letters, vol. 65, pp. 3152-3155, 1990

[2] E. Yablonovitch, T. J. Gmitter, and K. M. Leung, "Photonic Band Structure: The Face-Centered-Cubic Case Employing Nonspherical Atoms," Physical Review Letters, vol. 67, pp. 2295-2298, 1991.

[3] J. L. Jewell, J. P. Harbison, A. Scherer, Y. H. Lee, and L. T. Florez, "Vertical-Cavity Surface-Emitting Lasers: Design, growth, fabrication, characterization, "IEEE Journal of Quantum Electronics, vol. 27, pp. 1332-1346, 1991.

[4] Y. M. Houng, M. R. T. Tan, B. W. Liang, S. Y. Wang, and D. E. Mars, "In situ thickness monitoring and control for highly reproducible growth of distributed Bragg reflectors," Journal of Vacuum Science Technology B., vol. 12, pp.1221-1224, 1994.

[5] G. Tuttle, J. Kavanaugh, and S. McCalmont, "(Al,Ga)Sb long-wavelength distributed Bragg reflectors," IEEE Photonics Technology Letters, vol. 5, pp. 1376-1379, 1993.

[6] T. Krauss, Y. P. Song, S. Thomas, C. D. W. Wilkinson, and R. M. DelaRue, "Fabrication of 2-D photonic bandgap structures in GaAs/AlGaAs," Electronics Letters, vol. 30, pp. 1444-1446, 1994.

[7] K. M. Ho, C. T. Chan, C. M. Soukoulis, R. Biswas, and M. Sigalas, "Photonic Band Gaps in Three Dimensions: New Layer-by-Layer Periodic Structures," Solid State Communications, vol. 89, pp. 413-416, 1994.

[8] E. Ozbay and B. Temelkuran, "Reflection properties and defect formation in photonic crystals," Applied Physics Letters, vol. 69, pp. 743-745, 1996.

[9] G. Tuttle, J. S. McCalmont, M. Sigalas, R. Biswas, C. M. Soukoulis, and K. M. Ho, "Laser-Micromachined Millimeter-Wave Photonic Band-Gap Cavity Structures," Applied Physics Letters, vol. 67, pp. 1969-1971, 1995.

[10] R. S. Geels, S. W. Corzine, and L. A. Coldren. "InGaAs Vertical-Cavity Surface-Emitting Lasers," IEEE Journal of Quantum Electronics, vol. 27, pp. 1359-1367, June 1991.

[11] C. Lin, J. M. Meese, and Y. Chang, "A low-voltage high-reflectance-change normally off refractive GaAs/$Al_{0.2}Ga_{0.8}As$ MQW reflection modulator," IEEE Journal of Quantum Electronics, vol.30, pp.1234-1240, 1994.

[12] E. R. Brown and O. B. McMahon, "High zenithal directivity from a dipole antenna on a photonic crystal," Applied Physics Letters, vol. 68, pp. 1300-1302, 1996.

[13] Y. T. Lo and S. W. Lee, Antenna Handbook,, Vol 2, Van Nostrand Reinhold, New York, 1993.

[14] R. Yan, R. J. Simes, L. A. Coldren, "Analysis and Design of Surface-Normal Fabry-Perot Electrooptic Modulators," IEEE Journal of Quantum Electronics, vol.25, pp.2272-2280, 1989.

[15] B. Temelkuran, E. Ozbay, J. P. Kavanaugh, G. Tuttle, and K. M. Ho, "Resonant Cavity Enhanced Detectors Embedded in Photonic Crystals," Applied Physics Letters, vol. 72, pp. 2376-2378, 1998.

[16] J. Preissner, "The Influence of the Atmosphere on Passive Radiometric Measurements," AGARD Conference Reprint No. 245. Millimeter and Submillimeter Wave Propagation and Circuits, 1978.

[17] C. M. Soukoulis, Photonic Band Gap Materials,, Kluwer Academic Publishers, , Netherlands, 1996.

[18] N. G. Alexopoulos, P. B. Katehi, and D. B. Rutledge, "Substrate Optimization for Integrated Circuit Antennas," IEEE Transactions on Microwave Theory and Techniques, vol. MTT-31, pp. 550-557, 1983.

[19] J. G. Maloney, M. P. Kesler, B. L. Shirley, and G. S. Smith, "Simple description for waveguiding in photonic bandgap materials," Microwave and Optical Technology Letters, vol. 14, pp. 261-266, 1997.

[20] C. A. Balanis, Advanced Engineering Electromagnetics,, John Wiley & Sons, New York, 1989.

[21] P. L. Swart and B. M. Lacquet, "A New Algorithm For Layer Thickness and Index Step Estimation in Multi-Layer Hetero-Epitaxial Structures," Journal of Electronic Materials, vol. 19, pp. 1383-1394, 1990.

[22] K. W. Chang, H. Wang, G. Shreve, J. G. Harrison, M. Core, A. Paxton, M. Yu, C. H. Chen, and G. S. Dow, "Forward-Looking Automotive Radar Using a W-band Single-Chip Transceiver," IEEE Transactions on Microwave Theory and Techniques, vol. 43, pp. 1659-1668, 1995.